The Astrophysical Journal Supplement Series, 240:24 (19pp), 2019 February https://doi.org/10.3847/1538-4365/aaf8ba

The Southern H II Region Discovery Survey. I. The Bright Catalog

Trey V. Wenger[1,2], John. M. Dickey[3], C. H. Jordan[4,5], Dana S. Balser[2], W. P. Armentrout[6,7,8], L. D. Anderson[6,7,9], T. M. Bania[10], J. R. Dawson[11,12], N. M. McClure-Griffiths[13], and Jeanine Shea[2,14]
[1] Astronomy Department, University of Virginia, P.O. Box 400325, Charlottesville, VA 22904-4325, USA; tvw2pu@virginia.edu
[2] National Radio Astronomy Observatory, 520 Edgemont Road, Charlottesville, VA 22903, USA
[3] School of Natural Sciences, University of Tasmania, Hobart, TAS 7001, Australia
[4] International Centre for Radio Astronomy Research, Curtin University, Bentley, WA 6102, Australia
[5] ARC Centre of Excellence for All Sky Astrophysics in 3 Dimensions (ASTRO 3D), Australia
[6] Department of Physics and Astronomy, West Virginia University, Morgantown, WV 26505, USA
[7] Center for Gravitational Waves and Cosmology, West Virginia University, Morgantown, Chestnut Ridge Research Building, Morgantown, WV 26505, USA
[8] Green Bank Observatory, P.O. Box 2, Green Bank, WV 24944, USA
[9] Adjunct Astronomer at the Green Bank Observatory, P.O. Box 2, Green Bank, WV 24944, USA
[10] Institute for Astrophysical Research, Astronomy Department, Boston University, 725 Commonwealth Avenue, Boston, MA 02215, USA
[11] Department of Physics and Astronomy and MQ Research Centre in Astronomy, Astrophysics, and Astrophotonics, Macquarie University, NSW 2109, Australia
[12] Australia Telescope National Facility, CSIRO Astronomy and Space Science, P.O. Box 76, Epping, NSW 1710, Australia
[13] Research School of Astronomy and Astrophysics, Australian National University, Canberra, ACT 2611, Australia
[14] Department of Physics and Astronomy, Bucknell University, 153 Olin Science Building, Lewisburg, PA 17837, USA
Received 2018 September 18; revised 2018 December 11; accepted 2018 December 12; published 2019 January 31

Abstract

The census of Galactic H II regions is vastly incomplete in the southern sky. We use the Australia Telescope Compact Array to observe 4–10 GHz radio continuum and hydrogen radio recombination line (RRL) emission from candidate H II regions in the Galactic zone $259° < \ell < 344°$, $|b| < 4°$. In this first data release, we target the brightest H II region candidates and observe 282 fields in the direction of at least one previously known or candidate H II region. We detect radio continuum emission and RRL emission in 275 (97.5%) and 258 (91.5%) of these fields, respectively. We catalog the ∼7 GHz radio continuum peak flux densities and positions of 80 previously known and 298 candidate H II regions. After averaging ∼18 RRL transitions, we detect 77 RRL velocity components toward 76 previously known H II regions and 267 RRL velocity components toward 256 H II region candidates. The discovery of RRL emission from these nebulae increases the number of known Galactic H II regions in the surveyed zone by 82% to 568 nebulae. In the fourth quadrant, we discover 50 RRLs with positive velocities, placing those sources outside the solar circle. Including the pilot survey, the Southern H II Region Discovery Survey has now discovered 295 Galactic H II regions. In the next data release, we expect to add ∼200 fainter and more distant nebulae.

Key words: Galaxy: kinematics and dynamics – Galaxy: structure – H II regions – ISM: kinematics and dynamics – radio lines: ISM – surveys

Supporting material: machine-readable tables

1. Introduction

Massive OB-type stars ionize the natal gas in their surroundings, creating H II regions. Since these nebulae have short lifetimes ($\lesssim$10 Myr), they are the locations of current high-mass star formation in the Galaxy. H II regions are the classic tracer of Galactic spiral structure, and their chemical abundances reveal the metallicity of the interstellar medium in which they formed. A complete census of Galactic H II regions would inform models of both Galactic kinematics, as well as the formation and chemo-dynamical evolution of the Galaxy.

More than 60 years ago, Sharpless (1953, 1959) began surveys of Galactic H II regions. Starting with photographic plates from the 48" Schmidt telescope (now known as the Samuel Oschin Telescope) at the Palomar Observatory, Sharpless (1953) compiled a catalog of 142 "emission nebulae" and stars associated with those nebulae. Sharpless (1959) expanded upon his previous work using the newly completed National Geographic-Palomar Sky Atlas. Adopting the term "H II region" from Strömgren (1948), this second catalog contains 313 optical H II regions, covering the entire sky north of decl. −27°. Gum (1955), and later Rodgers et al. (1960), expanded the H II region survey to the southern hemisphere using Hα photographic plates from the Mount Stromolo Observatory.

With the prediction of radio recombination lines (RRLs) by Kardashev (1959) and their subsequent discovery by Hoglund & Mezger (1965a, 1965b), there was now an extinction-free spectroscopic tracer of optically obscured H II regions. The first generation of RRL H II region surveys was carried out by Reifenstein et al. (1970) and Wilson et al. (1970). Using the National Radio Astronomy Observatory (NRAO, now the Green Bank Observatory) 140 Foot telescope, Reifenstein et al. (1970) detected the H109α RRL toward 82 Galactic H II regions. Wilson et al. (1970) extended the survey to the southern sky using the NRAO 6 cm receiver on the 210 foot Parkes Telescope. They detected H109α RRL emission toward 130 Galactic H II regions, bringing the total census to 212 nebulae with RRL detections. These projects were successful despite the low spectral resolution (∼6 km s^{-1}) and high system temperatures (∼100 K) of their instruments.

Equipped with better telescopes, more sensitive receivers, and more advanced correlators, the second generation of surveys began with Downes et al. (1980) in the northern sky and Caswell & Haynes (1987) in the southern sky. Using the Effelsburg 100 m telescope, Downes et al. (1980) targeted 262 bright sources from the recently completed 5 GHz continuum survey by Altenhoff et al. (1979) in search of H110α RRL emission and H_2CO absorption. They detected RRL emission

toward 171 nebulae. Caswell & Haynes (1987) used the updated 1024-channel digital correlator on the Parkes telescope to simultaneously observe two RRLs (H109α and H110α), as well as H_2CO. By averaging the two RRL transitions, they were able to detect RRL emission from 316 Galactic H II regions. Using the NRAO 140 Foot telescope, Lockman (1989) observed all remaining reasonably bright compact radio continuum sources ($\gtrsim$1 Jy beam^{-1}) in the Altenhoff et al. (1979) survey. This generation of RRL surveys was completed by Lockman et al. (1996), who observed faint and diffuse radio sources in search of angularly large H II regions. These 140 Foot telescope surveys discovered approximately 350 new Galactic H II regions, bringing the total census of known Galactic H II regions to ~1000 nebulae.

With the completion of the Lockman (1989) and Lockman et al. (1996) surveys, all of the bright radio continuum sources in the Altenhoff et al. (1979) catalog were observed, and systematic searches for Galactic H II regions ceased. It was apparent, however, that the census of H II regions was vastly incomplete; only a handful of H II regions were known in the outer Galaxy in the first and fourth Galactic quadrants, for example. A deeper RRL survey would discover fainter and more distant H II regions, allowing us to explore both the Galactic structure and the properties of high-mass star formation beyond the Galactic Center.

We are now completing the third generation of RRL surveys of H II regions. This generation is motivated by two great advancements in the field: (1) deep all-sky infrared surveys, which are sensitive to the thermal dust emission associated with H II regions across the Galactic disk, and (2) ultra-sensitive radio telescopes with wide-bandpass receivers and correlators, which can simultaneously observe many RRL transitions. The Green Bank Telescope H II Region Discovery survey (GBT HRDS; Bania et al. 2010; Anderson et al. 2011) used the largest fully steerable telescope in the world to discover 448 new Galactic H II regions in the first and second Galactic quadrants. Follow-up surveys with the GBT and the Arecibo Telescope (Bania et al. 2012; Anderson et al. 2015, 2018) added another 439 H II regions, bringing the total number of HRDS discoveries to 887. These surveys more than doubled the number of known H II regions in the surveyed zone and completed the census of northern sky H II regions brighter than ~100 mJy beam^{-1} at ~9 GHz.

The Southern H II Region Discovery Survey (SHRDS) is an extension of the HRDS into the southern sky. Using the sensitive and wide-bandpass receivers on the Australia Telescope Compact Array (ATCA), we aim to complete the census of southern sky H II regions to nearly the same sensitivity limit as the HRDS (~100 mJy beam^{-1}). At the conclusion of the SHRDS, we will have a catalog of all Galactic H II regions ionized by at least a single O star. This catalog will reveal new insights into the current structure, formation, and evolutionary history of the Milky Way.

2. Target Sample

Our targets are selected from the *Wide-field Infrared Survey Explorer (WISE)* Catalog of Galactic H II Regions (Anderson et al. 2014). The *WISE* Catalog is the most complete census of known and candidate H II regions extant. Candidate H II regions are identified based on their spatially coincident 12 μm, 22 μm, and, if available, radio emission. The infrared data are taken from the *WISE* All-Sky data (Wright et al. 2010) and the radio data from the Multi-Array Galactic Plane Imaging Survey

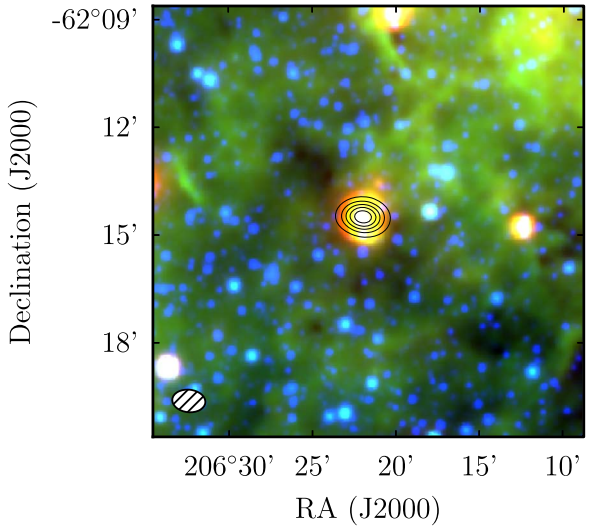

Figure 1. Infrared image of a typical H II region candidate from the *WISE* Catalog, G309.176−00.028. The image is a composite of *WISE* 22 μm (red), 12 μm (green), and 3.4 μm (blue) data. The black contours are the SHRDS 7 GHz continuum emission (50 mJy beam^{-1} to 250 mJy beam^{-1} in 50 mJy beam^{-1} intervals). The hatched ellipse represents the ATCA half-power synthesized beam.

(MAGPIS; Becker et al. 1994; Helfand et al. 2006), the Very Large Array Galactic Plane Survey (VGPS; Stil et al. 2006), the Canadian Galactic Plane Survey (CGPS; Taylor et al. 2003), the National Radio Astronomy Observatory Very Large Array Sky Survey (NVSS; Condon et al. 1998), the Southern Galactic Plan Survey (SGPS; (McClure-Griffiths et al. 2005), and the Sydney University Molonglo Sky Survey (SUMSS; Bock et al. 1999; Mauch et al. 2003). The 12 and 22 μm emission stems from the polycyclic aromatic hydrocarbons in the photodissociation region surrounding the H II region and the warm dust associated with the H II region, respectively. The radio emission is caused by thermal (free–free) emission from the ionized gas. The *WISE* Catalog contains about 8000 objects: ~2000 known H II regions, ~2000 radio-loud H II region candidates, and ~4000 radio-quiet H II region candidates. Radio-quiet H II region candidates are sources that have not been detected in existing radio continuum surveys. Figure 1 shows the *WISE* infrared image and SHRDS observed 7 GHz radio continuum contours for the H II region candidate, G309.176−00.028.

In this first data release, we target H II region candidates in the Galactic longitude range $259° < \ell < 344°$ with a predicted 6 GHz peak flux density greater than 60 mJy beam^{-1}. This longitude range contains the portion of the sky visible by the ATCA that could not be observed by the HRDS telescopes. We estimate the 6 GHz peak flux density by extrapolating from the measured SUMSS 843 MHz flux density, assuming $S_{6\,\mathrm{GHz}}/S_{843\,\mathrm{MHz}} = (6\,\mathrm{GHz}/843\,\mathrm{MHz})^{\alpha}$ with an optically thin spectral index of $\alpha = -0.1$. We also observe several previously known H II regions from the GBT HRDS, Caswell & Haynes (1987), and Wilson et al. (1970) catalogs. These observations allow us to test our data reduction and analysis procedure and to compare single-dish and interferometric results.

Our target list for the SHRDS Bright Catalog contains 257 H II region candidates and 25 previously known H II regions. In some cases, multiple targets are observable within one ATCA primary beam, so we group them into a single pointing, a "field," centered between the targets. We observe 282 individual fields that contain many more *WISE* Catalog sources than the 282

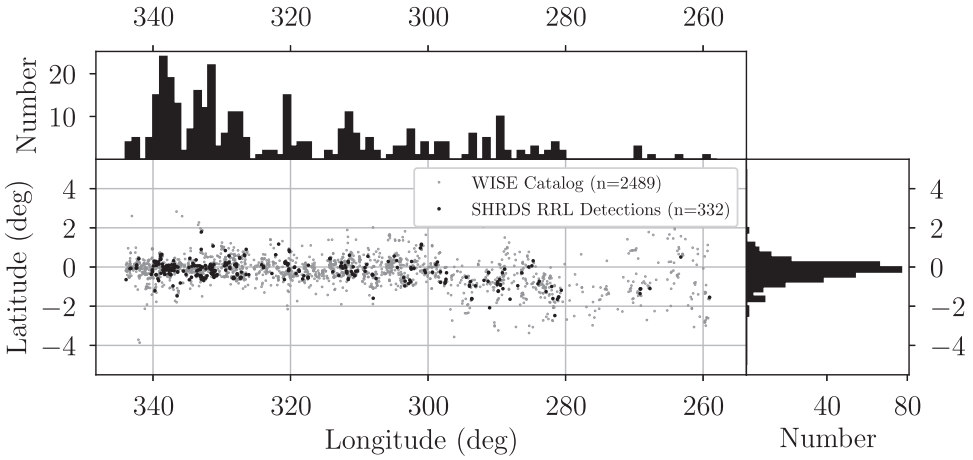

Figure 2. Galactic positions of all *WISE* Catalog H II regions and H II region candidates with $259° < \ell < 344°, |b| < 4°$ (gray points), as well as the subset of those observed in SHRDS fields (black points). The histograms show the Galactic distribution of the observed SHRDS targets.

Table 1
Bright Catalog Fields and Targets

Field	R.A. J2000 (hh:mm:ss)	Decl. J2000 (dd:mm:ss)	Epoch	Target[a]	Catalog[b]	R.A. J2000 (hh:mm:ss)	Decl. J2000 (dd:mm:ss)	R_{IR} (arcsec)	$S_{6\,GHz}$ (mJy beam^{-1})	$\Delta\theta$[c] (arcsec)	Author
shrds030	08:26:18.8	−40:48:36.5	2016	G259.013−01.546	Q	08:26:13.5	−40:46:45.0	68.08	⋯	⋯	
				G259.057−01.544^{T}	C	08:26:22.1	−40:48:49.4	103.98	135.54	39.81	
				G259.086−01.612	C	08:26:09.9	−40:52:36.1	103.98	⋯	⋯	
shrds035	08:37:05.6	−39:44:51.8	2015	G259.359+00.820	C	08:37:17.6	−39:39:30.3	500.76	94.64	350.65	
				G259.771+00.541	C	08:37:25.8	−40:09:15.3	3361.35	⋯	⋯	
shrds060	08:48:40.9	−42:53:10.3	2015	G263.237+00.509^{T}	C	08:48:44.0	−42:54:01.6	204.56	168.93	61.36	
shrds063	08:49:49.2	−43:09:37.3	2015	G263.554+00.656	C	08:50:27.3	−43:03:08.8	1043.51	43.67	568.91	
shrds073	08:52:41.6	−44:13:27.4	2015	G264.220+00.216	C	08:50:54.8	−43:50:47.4	1824.13	42.02	526.47	

Notes.
[a] "T" indicates that this source is a "nominal" target (see the text).
[b] The *WISE* Catalog designation: "K" is a known H II region, "C" is an H II region candidate, "Q" is a radio-quiet H II region candidate, and "G" is an H II candidate associated with an H II region group.
[c] The separation between the *WISE* Catalog infrared position and the position of the SUMSS continuum peak.
References. GBT HRDS (Anderson et al. 2011, 2015, 2018); CH87 (Caswell & Haynes 1987); L89 (Lockman 1989); W70 (Wilson et al. 1970).
(This table is available in its entirety in machine-readable form.)

bright targets. In total, there are 632 H II region candidates and 149 previously known H II regions within our fields, but most of these will be too distant and faint or too large and diffuse to be detected in our survey. Table 1 lists information about the H II regions and H II region candidates in each field. The field name, center position, and observing epoch are listed for each field. Each field contains multiple sources, and for each source we list the *WISE* Catalog source name; the *WISE* Catalog designation (K for previously known H II region, C for H II region candidate, Q for radio-quiet H II region candidate, and G for H II region candidate associated with a group of H II regions); the *WISE* infrared position; the *WISE* infrared radius, R_{IR}; the predicted 6 GHz peak continuum flux density, $S_{6\,GHz}$; the separation between the position of the SUMSS continuum peak emission and the infrared position, $\Delta\theta$; and the reference to the previously known RRL detection, if any. A superscript "T" on the source name indicates that this object meets our "nominal" target criteria: a predicted 6 GHz peak continuum flux density brighter than 60 mJy beam^{-1} and a predicted radio diameter smaller than the maximum recoverable scale of the ATCA at 6 GHz, which is ∼265 arcsec. We estimate that the radio diameter is half of the *WISE* Catalog infrared diameter (e.g., Bihr et al. 2016). There are 179 H II region candidates and 100 previously known H II regions in our fields that meet our nominal criteria. About 6% of our fields do not contain a nominal target due to a larger size criterion in our early observations. Figure 2 shows the positions of all *WISE* Catalog H II regions and H II region candidates with $259° < \ell < 344°$, as well as the subset of those observed in SHRDS fields.

3. Observations

We use the ATCA to observe radio continuum and hydrogen RRL emission in each field. The observing procedure and correlator configuration are similar to that used in the SHRDS pilot project (Brown et al. 2017). Data included here were observed 2015 June–October and 2016 July–September. In total, we observe 478 hr split nearly equally between the most compact H75 antenna configuration and the more extended H168 antenna configuration. A summary of the observing dates, hours observed, and antenna configurations is given in Table 2.

The *C/X*-band receiver on the ATCA covers 4–10 GHz with a ∼20 K system temperature. The Compact Array Broadband

Table 2
Observation Summary

Parameters	Epoch: 2015	Epoch: 2016
H75 Observing Dates	2015 Jul 24 to 2015 Aug 23	2016 Jul 23 to 2016 Aug 15
H75 Observing Time (hr)	121	150
H168 Observing Dates	2015 Sep 18 to 2015 Oct 14	2016 Sep 03 to 2016 Sep 29
H168 Observing Time (hr)	63	144
Total Observing Time (hr)	184	294
Primary Calibrators	0823−500, 1934−638	0823−500, 1934−638
Secondary Calibrators	0906−47, 1036−52, 1613−586, 1714−336, 1714−397, J1322−6532	1036−52, 1613−586, J1322−6532

Backend (CABB) simultaneously measures both low spectral resolution, large-bandwidth radio continuum spectral windows (hereafter, continuum windows), as well as many high spectral resolution, small-bandwidth spectral windows (hereafter, spectral line windows). We use CABB in the 64 MHz mode, which allows us to simultaneously observe two 2 GHz bandwidth continuum windows (4.5–6.5 GHz and 7.5–9.5 GHz) and thirty-two 64 MHz bandwidth spectral line windows. The continuum windows have 33 channels (64 MHz/channel) and the spectral line windows have 2048 channels (31.25 kHz/channel). We tune the spectral line windows to 20 different hydrogen RRLs, as summarized in Table 3. For each spectral window, we list the center frequency, $\nu_{\rm center}$; the bandwidth; the number of channels; and the channel width, $\Delta\nu$. For the spectral line windows, we also identify the targeted RRL and RRL rest frequency, $\nu_{\rm RRL}$. The data are observed in two circular polarizations, LL and RR, thus yielding 40 independent RRL spectra.

Our spectral window configuration is a compromise between the two setups used in the pilot survey. At lower frequencies, the RRLs are more tightly spaced in frequency, and we can observe more of them within a given bandwidth, but these RRLs are fainter and contaminated with more radio frequency interference (RFI). At higher frequencies, the RRLs are brighter, but they are more spaced out in frequency, and thus we observe fewer of them within a given bandwidth.

We use a two-phase observing strategy for the SHRDS: a first-pass "snapshot" survey in the H75 antenna configuration to measure the continuum brightness of each target, and then a second-pass "deep" survey split between the H75 and H168 antenna configurations to measure the RRLs. In the "snapshot" survey, we observe each target for a total of ∼20 minutes in ∼2–3 minute integrations spread over ∼9 hr in hour angle. We reduce these data and measure the continuum flux density of each target. Assuming an RRL-to-continuum intensity ratio of 0.10, which is typical for an optically thin H II region in local thermodynamic equilibrium at 6 GHz (e.g., Wilson et al. 1970; Lockman & Brown 1975), we estimate the integration time required to detect the RRL after averaging the 20 observed RRL transitions. We also take note of the level of confusion in each field, and we give confused fields priority in the H168 antenna configuration. In the "deep" survey, we re-observe each target for this estimated integration time split between the H75 and H168 antenna configurations.

Unlike the pilot survey, we aim to create high dynamic range images of our targets. Therefore, we require longer integrations and good coverage in the *uv*-plane. Total integration times on our targets range from ∼30 minutes to ∼60 minutes spread over ∼9 hr in the hour angle, depending on the predicted RRL intensity. Figure 3 shows an example of the typical *uv*-coverage for our observations. Our observing strategy nearly fills the *uv*-plane and yields high-fidelity, high dynamic range images. Due to the nature of an interferometer, however, we are not sensitive to any emission on spatial scales larger than the maximum recoverable scale of our most compact antenna configuration, which is ∼265 arcsec at 6 GHz. Since over 95% of the sources in the *WISE* Catalog have predicted radio sizes smaller than 265 arcsec, the ATCA is optimized for the SHRDS.

4. Data Reduction and Analysis

We developed a publicly available, modular data calibration, reduction, and analysis pipeline for the SHRDS: the Wenger Interferometry Software Package (WISP; Wenger 2018a, 2018b). The pipeline is written in *Python* and is implemented through the Common Astronomy Software Applications (CASA) package (McMullin et al. 2007). These tools are generic and may be used to reduce and analyze any continuum or spectral line interferometric data set. They benefit from a balance of automation and user-input with tunable parameters to handle multiple use cases. For example, the calibration pipeline uses built-in CASA automatic bad-data flagging algorithms, but also generates many data quality diagnostics used for manual flagging. Here, we briefly describe the specific calibration, reduction, and analysis steps used for the SHRDS. A more complete discussion of WISP and our data reduction process is in Appendix A.

4.1. Calibration

We observe at least one "primary" calibrator and several "secondary" calibrators each day. The primary calibrators, 0823–500 and 1934–638, are used to calibrate the absolute flux and delays and to remove instrumental bandpass structure. The secondary calibrators are point sources located close to our science targets on the sky and are used to calibrate the complex gains (phases and amplitudes) of our data. We typically observe a primary calibrator twice during a single observing session and a secondary calibrator every 10–20 minutes. Table 2 lists the calibrators we used in the Bright Catalog.

The calibration pipeline uses calibrator data to compute calibration solutions iteratively, to flag bad data automatically, to apply calibration solutions, and to flag bad data manually. We typically repeat this process two or three times for each observing session before the data are clear of all obvious RFI (or otherwise bad data) and the calibration solutions converge. The most common features we flag in the SHRDS data are (1) persistent RFI missed by the automatic flagging algorithms, (2) off-source antennas at the beginning of each scan, and (3) the first and last ∼200 channels of each spectral line window. Spectral window 17 (8060 MHz, see Table 3), covering H93α, is nearly always flagged due to persistent, broad-frequency RFI.

4.2. Imaging

Once the data from each observing session are fully calibrated, we create a single data set for each field, from which

Table 3
Correlator Setup

Window	$\nu_{\rm center}$ (MHz)	Bandwidth (MHz)	Channels	$\Delta\nu$ (kHz)	RRL	$\nu_{\rm RRL}$ (MHz)
0	5505	2112	33	64000	...	...
1	4609	64	2049	31.25	H112α	4618.790
2	4737	64	2049	32.25	H111α	4744.184
3	4865	64	2049	31.25	H110α	4874.158
4	4993	64	2049	31.25	H109α	5008.924
5	5153	64	2049	31.25	H108α	5148.704
6	5281	64	2049	31.25	H107α	5293.733
7	5441	64	2049	31.25	H106α	5444.262
8	5601	64	2049	31.25	H105α	5600.551
9	5761	64	2049	31.25	H104α	5762.881
10	5921	64	2049	31.25	H103α	5931.546
11	6113	64	2049	31.25	H102α	6106.857
12	6305	64	2049	31.25	H101α	6289.145
13	6465	64	2049	31.25	H100α	6478.761
14	8540	2112	33	64000	...	...
15	7548	64	2049	31.25	H95α	7550.616
16	7804	64	2049	31.25	H94α	7792.872
17	8060	64	2049	31.25	H93α	8045.604
18	8316	64	2049	31.25	H92α	8309.384
19	8572	64	2049	31.25	H91α	8584.823
20	9180	64	2049	31.25	H89α	9173.323
21	9500	64	2049	31.25	H88α	9487.823

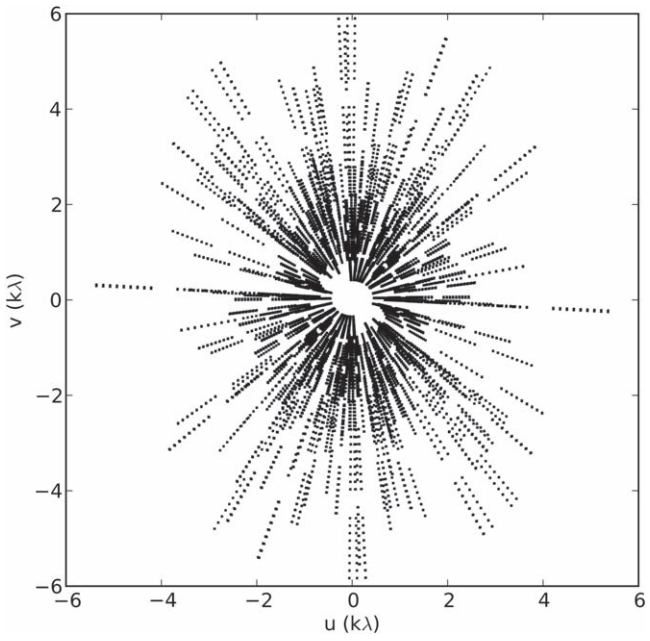

Figure 3. Representative example of the *uv*-coverage obtained for each SHRDS field. For clarity, only 9 of the 66 observed continuum window channels are shown. These data are the combination of $30 \sim 2$ minute snapshots split equally between the H75 and H168 antenna configurations.

we generate images. The imaging part of our data reduction and analysis pipeline is nearly fully automated (see Appendix A). We first regrid all of the visibilities to a common kinematic local standard of rest (LSR or LSRK[15]) velocity frame with a channel width of $\Delta v_{\rm LSR} = 2.5\,{\rm km\,s^{-1}}$. For each field, we then use the *CLEAN* algorithm to generate the following images and data cubes: (1) a multiscale, multifrequency synthesis (MS-MFS) image produced by combining the two 2 GHz continuum windows, (2) an MS-MFS image of each 2 GHz continuum window, (3) an MS-MFS image of each 64 MHz bandwidth spectral line window, and (4) a multiscale data cube of each spectral line window.

The emission mechanisms of H II regions allow us to take some shortcuts in our imaging process. The thermal radio continuum emission and RRL emission originate within the same volume of ionized gas. Thus, the morphology of the H II region should not change from channel to channel within a spectral line window. Therefore, to minimize computation time, we use the *CLEAN* masks from the MS-MFS images of each spectral line window to *CLEAN* that entire data cube. We also do not perform any continuum subtraction.

For resolved sources, we can increase the surface brightness sensitivity by *uv*-tapering our data. By giving less weight to the longer baselines when generating an image, *uv*-tapering increases the synthesized beam size and surface brightness sensitivity. Some fraction of our sources will be unresolved and/or in confused fields. In these cases, *uv*-tapering will worsen our point-source sensitivity and spatial resolution. Therefore, we generate two sets of images: one with no *uv*-tapering and a second with a *uv*-taper to a synthesized half-power beam width (HPBW) of 100 arcsec, which is approximately the synthesized HPBW of our lowest frequency spectral line window. Depending on the morphology of the source, the level of confusion within the field, and the scientific use, one of these methods may be more useful than the other.

4.3. Continuum Data Products

The radio continuum image provides several measurable quantities for each detected continuum source: the position, peak continuum flux density, total continuum flux density, and continuum spectral index. In this first data release, we only extract the positions and peak continuum flux densities of our continuum detections associated with *WISE* Catalog H II

[15] LSRK is defined by a solar motion of $20\,{\rm km\,s^{-1}}$ in the direction (R.A., decl.) = ($18^{\rm h}$, +30°) at epoch 1900.

Table 4
Non-tapered Image Continuum Properties

Target	R.A. J2000 (hh:mm:ss)	Decl. J2000 (dd:mm:ss)	Field	Epoch[a]	Beam Area (arcsec^2)	$\Delta\theta$[b] (arcsec)	ν_C (MHz)	S_C (mJy beam^{-1})	rms$_C$ (mJy beam^{-1})	QF
G213.833+00.618	06:55:16.9	+0:31:12.3	g213.833+00.618	2014*	⋯	2.5	⋯	⋯	⋯	⋯
G230.354−00.597	07:21:49.5	−15:44:09.9	g230.354-00.597	2014*	⋯	2.2	⋯	⋯	⋯	⋯
G259.057−01.544	08:26:18.1	−40:48:36.0	shrds030	2016	1353	47.4	7022	69.76	0.31	B
G259.359+00.820	08:37:05.3	−39:44:47.8	shrds035	2015	2501	347.8	7022	19.62	0.06	A
G263.237+00.509	08:48:37.6	−42:53:54.1	shrds060	2015	3077	70.1	7022	67.53	0.43	B
G264.681+00.272	08:52:55.7	−44:16:11.3	shrds073	2015	1382	385.2	7022	2.94	0.23	C
G265.191−00.641	08:50:38.3	−45:08:20.4	shrds075	2015	2479	17.1	7022	56.13	0.31	B
G267.730−01.100	08:58:04.5	−47:22:51.2	shrds078	2016	1627	12.2	7023	226.76	8.29	A

Notes.
[a] Rows with epochs with an asterisk (*) are copied directly from Brown et al. (2017). They did not give the continuum fluxes for their detections.
[b] The separation between the *WISE* Catalog infrared position and the position of the SHRDS continuum peak.

(This table is available in its entirety in machine-readable form.)

Table 5
uv-tapered Image Continuum Properties

Target	R.A. J2000 (hh:mm:ss)	Decl. J2000 (dd:mm:ss)	Field	Epoch[a]	Beam Area (arcsec^2)	$\Delta\theta$[b] (arcsec)	ν_C (MHz)	S_C (mJy beam^{-1})	rms$_C$ (mJy beam^{-1})	QF
G213.833+00.618	06:55:16.9	+0:31:12.3	g213.833+00.618	2014*	⋯	2.5	⋯	⋯	⋯	⋯
G230.354−00.597	07:21:49.5	−15:44:09.9	g230.354-00.597	2014*	⋯	2.2	⋯	⋯	⋯	⋯
G259.057−01.544	08:26:19.2	−40:48:32.2	shrds030	2016	9022	37.8	7022	192.46	0.98	B
G259.359+00.820	08:37:05.6	−39:44:47.7	shrds035	2015	9230	346.0	7022	20.98	0.13	A
G263.237+00.509	08:48:38.4	−42:53:58.1	shrds060	2015	9205	61.8	7022	149.64	0.89	A
G264.681+00.272	08:52:50.5	−44:13:51.4	shrds073	2015	8244	237.1	7022	4.91	1.88	C
G265.191−00.641	08:50:38.6	−45:08:12.4	shrds075	2015	9233	19.1	7022	61.11	0.73	B
G267.730−01.100	08:58:04.4	−47:22:55.2	shrds078	2016	8498	15.1	7023	404.28	32.87	A

Notes.
[a] Rows with epochs with an asterisk (*) are copied directly from Brown et al. (2017). They did not give the continuum fluxes for their detections.
[b] The separation between the *WISE* Catalog infrared position and the position of the SHRDS continuum peak.

(This table is available in its entirety in machine-readable form.)

regions and H II region candidates. In a future data release, we will publish the total continuum flux densities and continuum spectral indicies as well.

We use the 8–10 GHz MS-MFS continuum band image to identify continuum sources within our primary beam. Although the full 4 GHz bandwidth continuum image has better sensitivity, the 8–10 GHz image has better spatial resolution. This higher-frequency image will reveal more structure in confused fields. In each field, we identify distinct continuum emission peaks by visual inspection. Each distinct continuum peak is what we call a "continuum source." In this data release, we only identify continuum sources associated with *WISE* Catalog H II regions or H II region candidates. To be a continuum source in our Bright Catalog, we require that the continuum peak be within a circle centered on the *WISE* Catalog position with a radius equal to the infrared radius.

4.4. RRL Data Products

Our goal here is to create a catalog of H II region positions and RRL LSR velocities. We maximize our spectral sensitivity by averaging every H$n\alpha$ RRL transition and both polarizations to create a stacked H$n\alpha$ spectrum, denoted by $\langle \mathrm{H}n\alpha \rangle$. Upon the completion of the entire SHRDS, we will publish the spectra for each detected individual RRL transition.

We extract and average spectra from our data in two ways, depending on whether the data cube is *uv*-tapered or not. For non-tapered data cubes, we extract spectra from each of our spectral windows at the location of the peak continuum source brightness. We remove all poor-quality spectra, usually caused by unflagged RFI or a very poor baseline structure, then we use a weighted average to create the $\langle \mathrm{H}n\alpha \rangle$ spectrum. The weights for the ith spectral line window are given by $w_i = S_{C,i}/\mathrm{rms}_i^2$, where $S_{C,i}$ is the continuum brightness, and rms_i is the spectral noise of the ith spectral line window. Both the continuum brightness and rms noise are estimated from the line-free regions of the spectrum. For *uv*-tapered data cubes, we first smooth each of the spectral window cubes to a common beam size that is slightly larger than the *uv*-tapered beam size (typically 110 arcsec). After removing spectral windows with poor-quality spectra, we average the remaining cubes to create the $\langle \mathrm{H}n\alpha \rangle$ cube using the same weighting scheme as with the non-tapered data. We extract the $\langle \mathrm{H}n\alpha \rangle$ spectrum at the location of the peak continuum source brightness.

For each $\langle \mathrm{H}n\alpha \rangle$ spectrum, we identify the line-free regions and use those to estimate the spectral rms noise and to fit and subtract a third-order polynomial baseline. We then fit a single Gaussian line profile to the spectrum to measure the RRL brightness, the FWHM line width, the LSR velocity, and the signal-to-noise ratio (S/N). We estimate the S/N following the Lenz & Ayres (1992) method:

$$\mathrm{S/N} = 0.7\left(\frac{S_L}{\mathrm{rms}}\right)\left(\frac{\Delta V}{\Delta v}\right)^{0.5}, \quad (1)$$

where S_L is the peak line intensity, rms is the spectral noise, ΔV is the FWHM line width, and Δv is the channel width (2.5 km s^{-1}). In cases where multiple RRL components are visible, we fit multiple Gaussian profiles.

5. SHRDS: The Bright Catalog

The SHRDS Bright Catalog contains the radio continuum and $\langle \mathrm{H}n\alpha \rangle$ RRL properties of the brightest H II regions in the survey. We observe 282 fields containing 149 previously known H II regions and 632 H II region candidates in the Galactic longitude range of $259° < \ell < 344°$. The majority of these objects are too faint or too large to be detected by the ATCA. They are serendipitously observed because they are close to bright H II regions and H II region candidates on the sky. We detect at least 1 radio continuum source in 275 fields (97.5%) and at least 1 $\langle \mathrm{H}n\alpha \rangle$ RRL in 258 fields (91.5%). We find radio continuum and $\langle \mathrm{H}n\alpha \rangle$ RRL emission toward 80 and 76 previously known H II regions, respectively, and toward 298 and 256 H II region candidates, respectively. If instead we consider our "nominal" targets (H II region candidates with predicted 6 GHz peak continuum flux densities brighter than 60 mJy beam^{-1} and predicted radio diameters less than 265 arcsec, or known H II regions with predicted radio diameters less than 265 arcsec), there are only 100 previously known H II regions and 279 H II region candidates in our fields. Of these, we detect radio continuum emission toward 72 (72%) previously known H II regions and 246 (88%) H II region candidates. We also find RRL emission toward 76 (76%) previously known H II regions and 230 (82%) H II region candidates. Many of these sources lie near the edge of our primary beam, which further decreases our detection rates.

In this catalog, we also include data from the SHRDS pilot survey (Brown et al. 2017). We attempt to reprocess these data using WISP with mixed success. The fields observed in the SHRDS pilot survey did not typically have adequate *uv*-coverage to create high-fidelity images. Rather, Brown et al. (2017) extracted spectra directly from the *uv* data and averaged them to create the $\langle \mathrm{H}n\alpha \rangle$ spectra. They report detections of $\langle \mathrm{H}n\alpha \rangle$ RRL emission from 7 previously known H II regions and 36 out of 53 H II region candidates. In our reprocessed pilot survey data, we find continuum emission from 7 previously known H II regions and 46 H II region candidates and $\langle \mathrm{H}n\alpha \rangle$ RRL emission from 7 previously known H II regions and 26 H II region candidates. Nearly all of our detections are from the first epoch (2013) of the SHRDS pilot survey, simply due to the better *uv*-coverage of the first epoch observations. Our reprocessing discovers $\langle \mathrm{H}n\alpha \rangle$ RRL emission from four previously known H II regions and one H II region candidate not in the pilot survey catalog. These sources are not in the center of the field and thus were missed by the *uv*-spectra averaging method used by Brown et al. (2017). In the following catalogs, we list our re-analyzed products, if available; otherwise, we give the values from Brown et al. (2017). Data

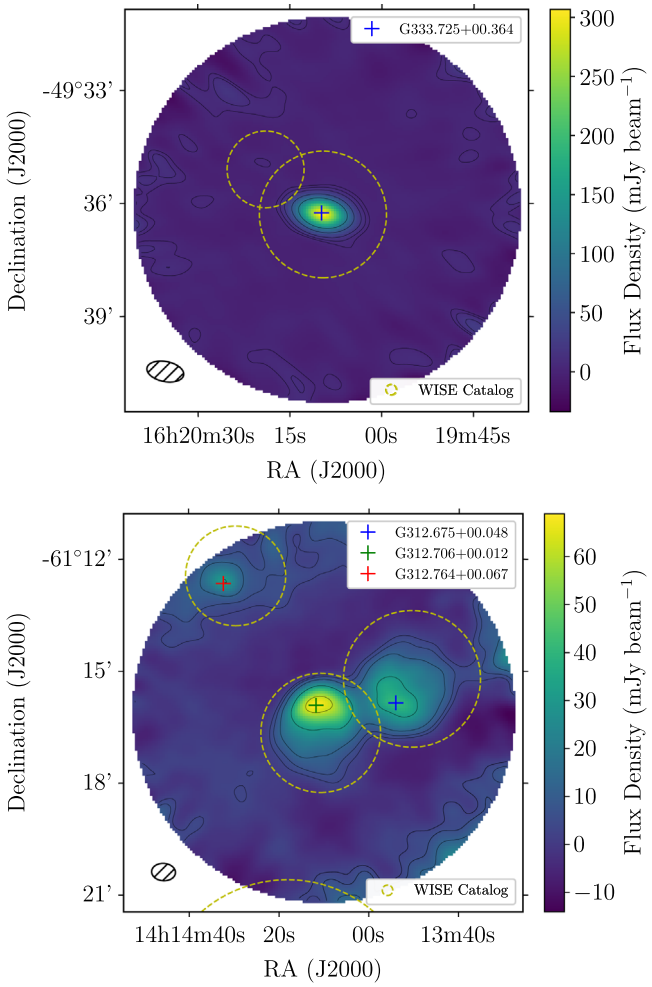

Figure 4. Representative 8–10 GHz continuum band images for each continuum quality factor (QF). The top panel is field "shrds803" (non-tapered), which contains a continuum QF A target, G333.725+00.364 (unresolved, unconfused, and centered). The bottom panel is field "shrds462" (non-tapered), which contains two continuum QF B targets, G312.706+00.012 and G312.675 +00.048 (resolved and spatially confused), as well as a QF C target, G312.764 +00.067 (resolved and far off-center). The black contours are 5, 10, 20, 50, and 100 times the field center rms noise. The yellow dashed circles represent infrared positions and sizes of the objects in the *WISE* Catalog, the crosses are the locations of the peak continuum emission, and the hatched ellipse represents the ATCA half-power synthesized beam at 7 GHz.

taken directly from Brown et al. (2017) have an asterisk (*) appended to the epoch. Three of the pilot survey "previously known" H II regions (G290.323−02.984, G295.748−00.207, and G323.464+00.079) did not have previous detections of Hα or RRL emission, so they are listed as candidate H II regions in the *WISE* Catalog. These sources are new SHRDS H II region discoveries.

5.1. Continuum Catalog

Our continuum source detections are listed in Table 4 (non-tapered) and Table 5 (*uv*-tapered). For each source, we list the *WISE* Catalog name; the position of the peak radio continuum emission; the field containing the source; the epoch; the synthesized beam area in the continuum image; the separation between the observed continuum peak position and infrared position, $\Delta\theta$; the MFS-synthesized frequency of the continuum image, ν_C; the peak continuum flux density, S_C; the rms noise, rms_C; and a "quality factor." The peak continuum flux density

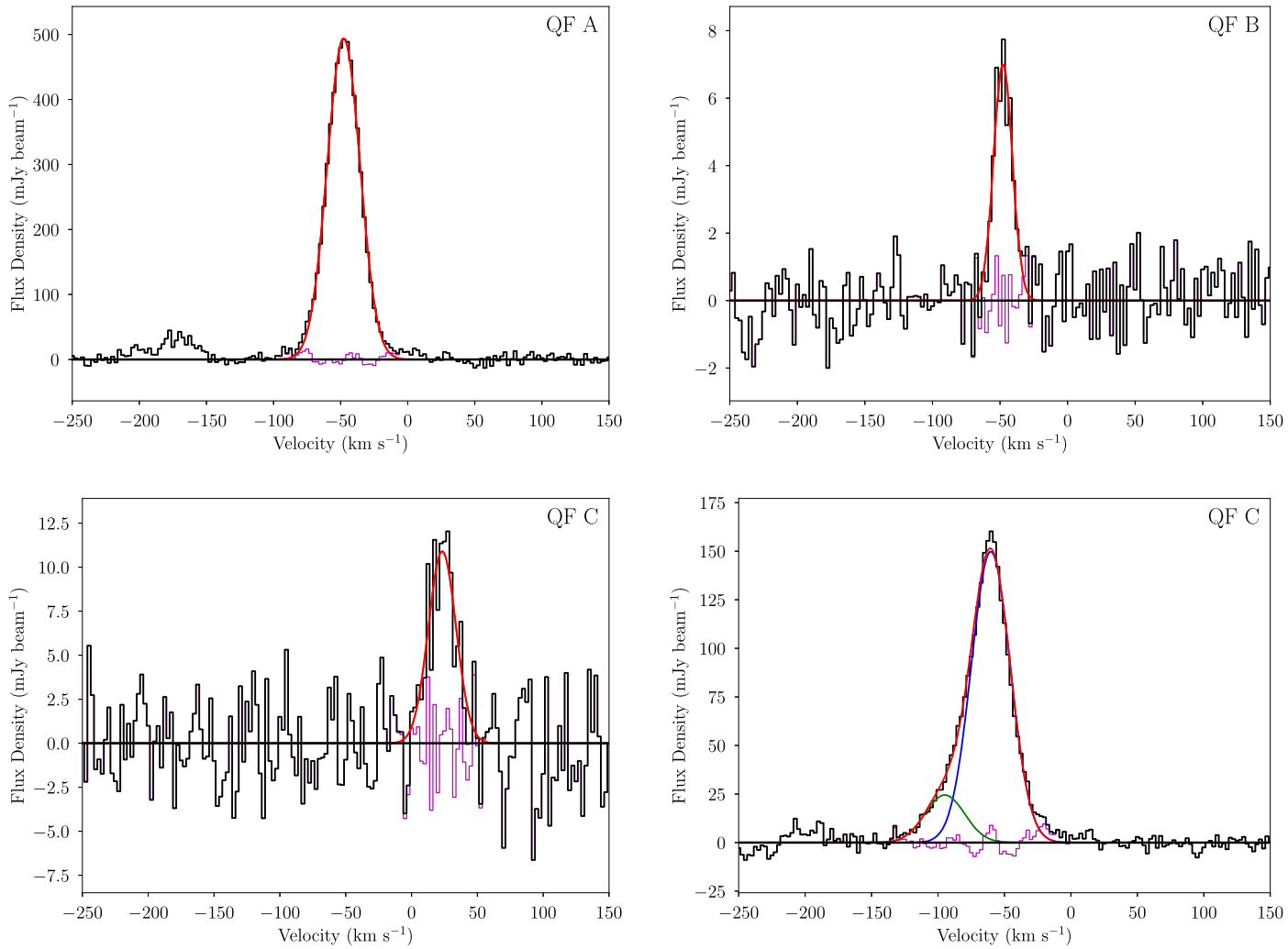

Figure 5. Representative $\langle \mathrm{H}n\alpha \rangle$ spectra for each spectral quality factor (QF). The top left panel is G333.129−00.439 and is a QF A spectrum (S/N > 15, unblended), the top right is G312.979−00.432 and is a QF B spectrum (15 > S/N > 10), the bottom left panel is G311.866−00.238 and is a QF C spectrum (S/N < 10), and the bottom right is G332.823–00.550 and is a QF C spectrum (spectrally blended). The red curves are Gaussian fits to the data (or the sum of the two Gaussian components in G332.823–00.550), and the magenta curves are the fit residuals.

Table 6
Non-tapered Image RRL Properties

Target	Field	Epoch[a]	ν_L[b] (MHz)	S_L (mJy beam^{-1})	V_{LSR} (km s^{-1})	ΔV (km s^{-1})	rms$_L$ (mJy beam^{-1})	S/N	QF
G213.833+00.618	g213.833+00.618	2014*	⋯	1.90 ± 2.30	53.20 ± 20.20	33.50 ± 20.90	1.40	3.5	C
G230.354−00.597	g230.354-00.597	2014*	⋯	2.10 ± 2.00	69.00 ± 16.10	35.00 ± 16.70	1.50	3.7	C
G259.057−01.544	shrds030	2016	6474	5.20 ± 0.40	59.20 ± 1.10	26.80 ± 2.60	1.10	10.9	B
G263.237+00.509	shrds060	2015	6338	8.10 ± 1.10	10.40 ± 1.20	17.50 ± 2.70	1.90	7.8	C
G267.730−01.100	shrds078	2016	6928	26.50 ± 0.70	7.30 ± 0.30	21.50 ± 0.60	1.50	36.6	A
G269.068−01.114	shrds085	2016	6028	75.70 ± 1.50	13.20 ± 0.20	25.00 ± 0.60	3.40	49.4	A
G269.159−01.119	shrds085	2016	6513	28.80 ± 0.70	10.70 ± 0.30	25.90 ± 0.80	1.80	36.3	A
G269.167−01.357	shrds086	2016	6445	7.30 ± 0.50	2.80 ± 0.80	23.90 ± 1.90	1.00	16.1	A

Notes.
[a] Rows with epochs with an asterisk (*) are copied directly from Brown et al. (2017). They did not give the weighted-average frequency of their H$n\alpha$ RRL spectra.
[b] This is the weighted-average frequency of the $\langle \mathrm{H}n\alpha \rangle$ stacked spectrum.

(This table is available in its entirety in machine-readable form.)

and position are measured at the location of the brightest pixel of the continuum source in the 4 GHz bandwidth MS-MFS continuum image. The rms noise is estimated as the rms across the entire residual image divided by the primary beam response at the continuum source position. The quality factor, QF, is a qualitative assessment of the accuracy of the peak continuum

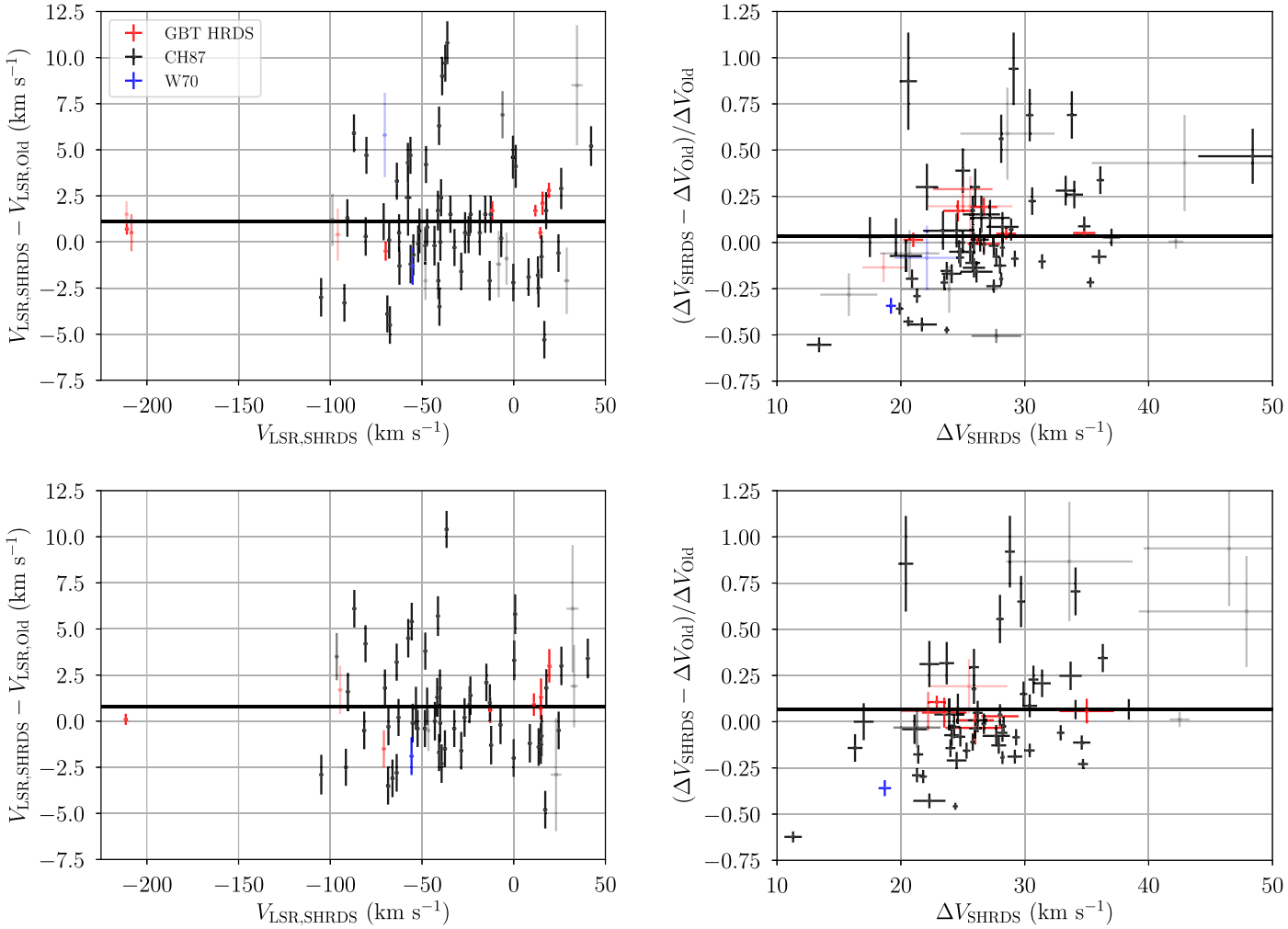

Figure 6. Differences between SHRDS and previously measured $\langle {\rm H}n\alpha \rangle$ LSR velocities, $V_{\rm LSR}$ (left), and fractional differences between SHRDS and previously measured FWHM line widths, ΔV (right). The top two panels use the non-tapered data and the bottom two panels use the *uv*-tapered data. Previous RRL measurements are from the GBT HRDS (red; $n = 10$ non-tapered; $n = 8$ tapered), Caswell & Haynes (1987; CH87; black; $n = 63$ non-tapered; $n = 56$ tapered), and Wilson et al. (1970); W70; blue; $n = 2$ non-tapered; $n = 1$ tapered). The transparency of the points represents the quality factor of the SHRDS RRL detection: QF A (not transparent), QF B (partially transparent), and QF C (mostly transparent). Six non-tapered SHRDS detections and five *uv*-tapered detections with LSR velocities more than 15 km s^{-1} different from the Caswell & Haynes (1987) velocities are excluded. The mean of each sample is indicated by the horizontal solid line.

Table 7
uv-tapered Image RRL Properties

Target	Field	Epoch[a]	ν_L[b] (MHz)	S_L (mJy beam^{-1})	$V_{\rm LSR}$ (km s^{-1})	ΔV (km s^{-1})	rms$_L$ (mJy beam^{-1})	S/N	QF
G213.833+00.618	g213.833+00.618	2014*	⋯	1.90 ± 2.30	53.20 ± 20.20	33.50 ± 20.90	1.40	3.5	C
G230.354−00.597	g230.354-00.597	2014*	⋯	2.10 ± 2.00	69.00 ± 16.10	35.00 ± 16.70	1.50	3.7	C
G259.057−01.544	shrds030	2016	6295	10.80 ± 0.80	58.00 ± 0.90	24.50 ± 2.10	2.10	11.3	B
G263.237+00.509	shrds060	2015	6196	16.90 ± 1.30	11.10 ± 0.60	17.20 ± 1.50	2.30	13.5	B
G267.730−01.100	shrds078	2016	6447	32.40 ± 1.30	7.70 ± 0.40	22.70 ± 1.00	2.30	29.6	A
G269.068−01.114	shrds085	2016	6127	149.70 ± 3.20	13.60 ± 0.20	23.70 ± 0.60	6.10	52.8	A
G269.159−01.119	shrds085	2016	6411	53.40 ± 1.50	11.00 ± 0.30	23.60 ± 0.80	3.10	37.1	A
G269.167−01.357	shrds086	2016	6515	22.00 ± 1.00	3.20 ± 0.50	22.10 ± 1.20	2.10	22.3	A

Notes.
[a] Rows with epochs with an asterisk (*) are copied directly from Brown et al. (2017). They did not give the weighted-average frequency of their H$n\alpha$ RRL spectra.
[b] This is the weighted-average frequency of the $\langle {\rm H}n\alpha \rangle$ stacked spectrum.

(This table is available in its entirety in machine-readable form.)

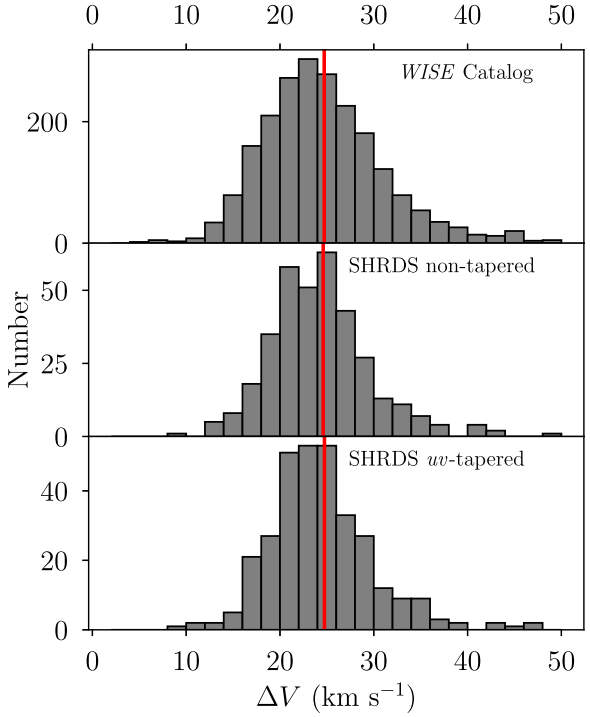

Figure 7. Distribution of $\langle \mathrm{H}n\alpha \rangle$ RRL FWHM line widths, ΔV, for all previously known H II regions in the *WISE* Catalog (top; $n = 2148$), SHRDS non-tapered detections (middle; $n = 353$), and SHRDS *uv*-tapered detections (bottom; $n = 317$), excluding 16 sources from the *WISE* Catalog and 2 sources from the SHRDS with $\Delta V > 50$ km s^{-1}. The mean of each sample is indicated by the vertical red line: 24.7 km s^{-1} for the *WISE* Catalog, 24.6 km s^{-1} for the non-tapered SHRDS, and 24.7 km s^{-1} for the *uv*-tapered SHRDS.

flux density. QF A means the source is unresolved, unconfused, and located near the center of the primary beam; QF B means the source is slightly resolved, slightly confused, and/or located off-center; and QF C means the source is very resolved, very confused, and/or located near the edge of the primary beam. The primary beam shape is not modeled accurately by CASA beyond ∼300 arcsec from the field center, so continuum sources near the primary beam edge may have flux density errors of $\gtrsim$10% (see Appendix A). Figure 4 shows representative 8–10 GHz continuum band images for each QF: G333.725+00.364 (QF A), G312.706+00.012 and G312.675+00.048 (QF B), and G312.764+00.067 (QF C).

A given *WISE* Catalog source may appear in multiple fields. These cases, which we call "multiple detections," nonetheless have only a single entry in Tables 4 and 5. The data for these targets have the highest continuum QF and/or the largest peak continuum flux-to-rms ratio. Every field is an independent observation of the source; however, we give the continuum properties as measured in each field in Appendix B. In the next data release, we will combine the data from each field to improve our sensitivity and to measure the continuum properties of these sources more accurately.

5.2. RRL Catalog

We list the RRL emission properties for detected sources in Table 6 (non-tapered $\langle \mathrm{H}n\alpha \rangle$) and Table 7 (*uv*-tapered $\langle \mathrm{H}n\alpha \rangle$). For each source, we give the *WISE* Catalog name; the field; the epoch; the weighted-average frequency of the $\langle \mathrm{H}n\alpha \rangle$ RRL, ν_L; the Gaussian fits to the peak line intensity, S_L; LSR velocity, V_{LSR}; the FWHM line width, ΔV; the rms spectral noise in the line-free region of the spectrum, rms_L; the signal-to-noise ratio calculated using Equation (1), S/N; and a QF. Like those assigned in the continuum catalog, the QFs are qualitative assessments of the accuracy of the Gaussian fits. Some of the $\langle \mathrm{H}n\alpha \rangle$ spectra show multiple RRL components. These components may be distinct in velocity but they are often spectrally blended. QF A means the RRL is unblended with an S/N > 15. QF B means the RRL is partially blended but has distinct peaks and/or has 15 > S/N > 10. QF C means the RRL is very blended with no distinct peaks and/or has S/N < 10. Finally, QF D is assigned to spectra with no visible RRL. Figure 5 shows example $\langle \mathrm{H}n\alpha \rangle$ spectra for each QF: G333.129–00.439 (QF A), G312.979–00.432 (QF B), and G311.866–00.238 and G332.823–00.550 (QF C). Sources with multiple RRL components have multiple rows in the tables, and the *WISE* Catalog name is appended by a letter, with "a" being the brightest RRL component, "b" being the second brightest, and so on.

We have multiple detections of RRLs for sources observed in separate fields. Tables 6 and 7 only contain the $\langle \mathrm{H}n\alpha \rangle$ Gaussian fits with the highest RRL QF and/or S/N. The data for these sources, as measured in each independent field, are listed in Appendix B. In the next data release, we will combine the $\langle \mathrm{H}n\alpha \rangle$ spectra from each field to increase our spectral sensitivity.

6. Properties of Bright Catalog Nebulae

For the longitude range $259° < \ell < 344°$, the SHRDS Bright Catalog increases the number of known Galactic H II regions to 568 nebulae, an 82% increase in the H II region census of this Galactic zone. With such a large sample of H II regions in the third and fourth Galactic quadrants, we can begin to get a global view of star formation and Galactic structure across the entire disk.

To assess the validity of our data reduction and analysis pipeline, we compare our measured RRL properties with those in the *WISE* Catalog for 76 previously known H II regions, 25 of which were re-observed by the SHRDS for this purpose. Figure 6 shows the difference between the SHRDS and previously measured $\langle \mathrm{H}n\alpha \rangle$ LSR velocities and FWHM line widths as a function of the SHRDS-measured values, for both the non-tapered and *uv*-tapered SHRDS data. These figures exclude six non-tapered and five *uv*-tapered SHRDS detections with LSR velocities more than 15 km s^{-1} different from the Caswell & Haynes (1987) velocities. These sources are G289.806−01.242, G300.502–00.180 (non-tapered only), G311.841−00.219, G311.866−00.238, G324.924−00.569, and G333.681−00.441. Each of these nebulae are near an extended H II region or an H II region complex with many other nebulae. We suspect that the Caswell & Haynes (1987) single-dish survey is more sensitive to the larger H II regions, and thus some LSR velocities are incorrectly assigned to these smaller, nearby H II regions in the *WISE* Catalog.

The SHRDS LSR velocities match previous measurements fairly well. The LSR velocity differences are clustered around 0 km s^{-1} with slightly more scatter toward larger SHRDS velocities. The mean velocity difference is 1.1 ± 0.4 km s^{-1} with a standard deviation of 3.2 km s^{-1} for the non-tapered sample. For the *uv*-tapered sample, the mean difference is 0.8 ± 0.3 km s^{-1} with a standard deviation of 2.8 km s^{-1}. This scatter is comparable to the spectral resolution of the SHRDS and the Caswell & Haynes (1987) survey (∼2.5 km s^{-1}).

Similarly, the FWHM line width differences are centered around zero with more scatter toward larger SHRDS line widths, some of which are nearly a factor of two larger than

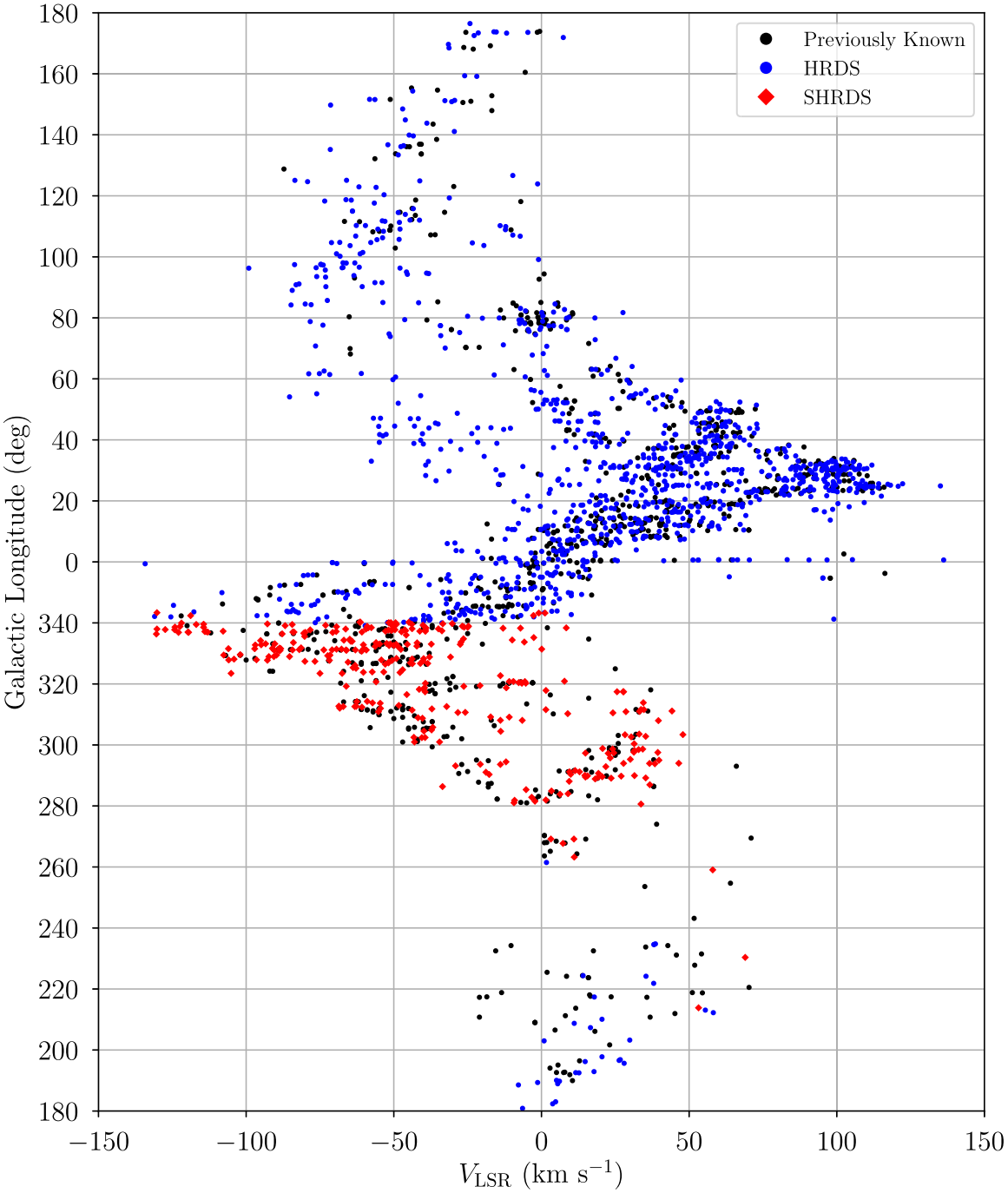

Figure 8. Galactic longitude, ℓ, as a function of LSR velocity, $V_{\rm LSR}$, for all known Galactic H II regions with $|V_{\rm LSR}| < 150$ km s^{-1}. Black points are H II regions known prior to the GBT HRDS, blue points are H II regions discovered by the GBT and Arecibo HRDS and their extensions, and red diamonds are H II regions in the SHRDS Bright Catalog.

previous measurements. We compute the fractional difference between the SHRDS-measured FWHM line width, $\Delta\nu_{\rm SHRDS}$, and the previously measured value, $\Delta\nu_{\rm Old}$, as $(\Delta\nu_{\rm SHRDS} - \Delta\nu_{\rm Old})/\Delta\nu_{\rm Old}$. The mean FWHM line width fractional difference is $3 \pm 3\%$ with a standard deviation of 30% for the non-tapered sample and is $7 \pm 8\%$ with a standard deviation of 32% for the *uv*-tapered sample. The large scatter in the line widths is probably an artifact of the different spatial scales probed by an interferometer and a single-dish telescope.

There is no difference in the distribution of $\langle {\rm H}n\alpha \rangle$ RRL FWHM line widths in the SHRDS and those in the *WISE* Catalog, nor a difference between the non-tapered and *uv*-tapered FWHM line width distributions. Figure 7 shows the RRL line widths of all known H II regions with RRL measurements in the *WISE* Catalog and all of the RRL line widths measured in the SHRDS, both non-tapered and *uv*-tapered. Each distribution peaks near $\sim$23 km s^{-1} and has a long tail toward large FWHMs. The mean FWHM line widths are 25 km s^{-1} in each sample. The similarity of the SHRDS and *WISE* Catalog line width distributions implies that the physical conditions (e.g., internal turbulence) of H II regions are comparable between the SHRDS survey zone and the rest of the Galaxy.

The Galactic longitude–velocity (ℓ-v) diagram that includes the nebulae discovered here shows interesting structure in the

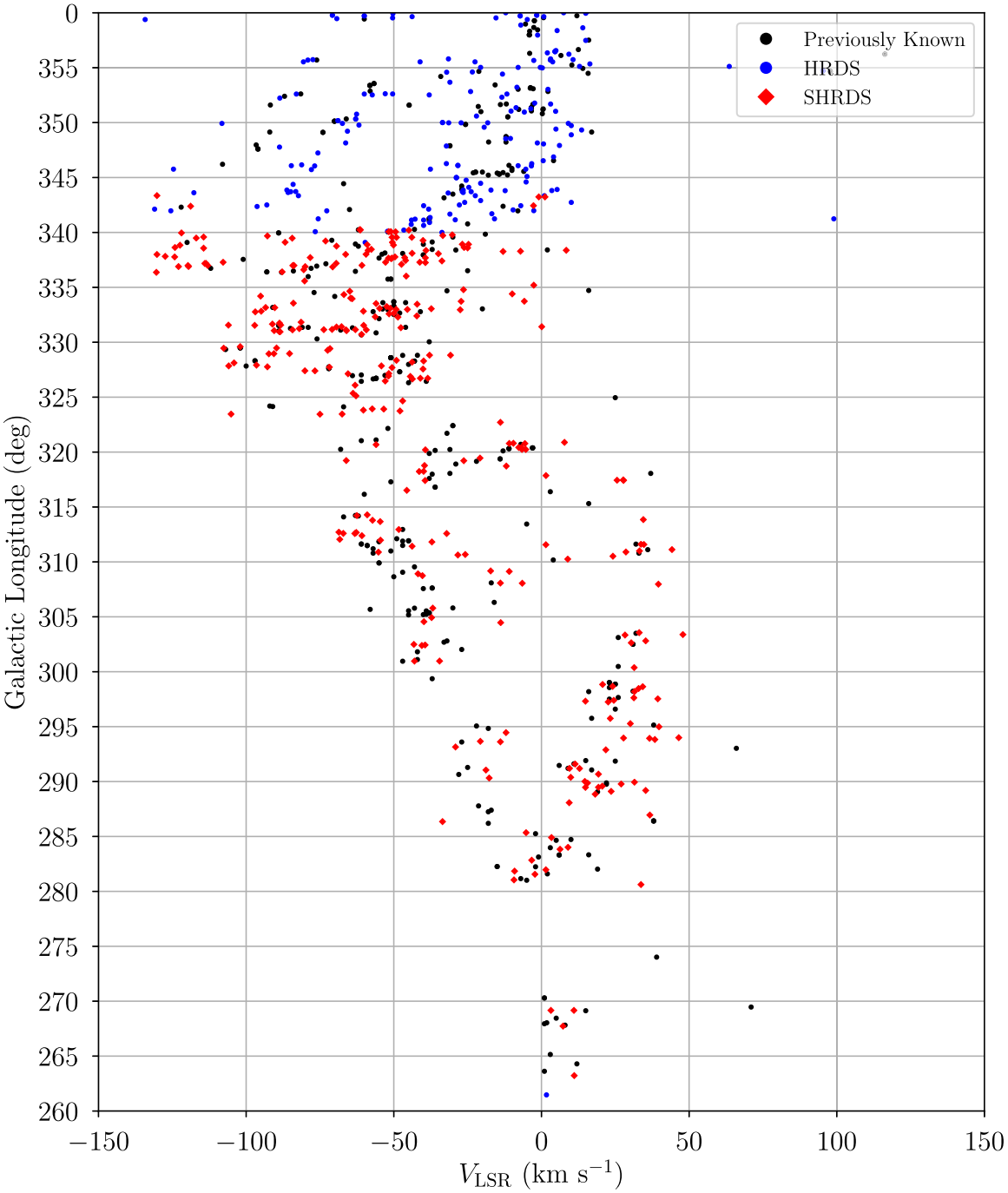

Figure 9. Same as Figure 8, but zoomed-in on the fourth Galactic quadrant.

fourth Galactic quadrant. Figure 8 is the ℓ-v diagram of all previously known and SHRDS-discovered H II regions with LSR velocities $|V_{\rm LSR}| < 150$ km s^{-1}, and Figure 9 is zoomed-in on the fourth Galactic quadrant. The SHRDS nebulae are constrained to $V_{\rm LSR} < 50$ km s^{-1} in the fourth quadrant, which is likely due to a lack of sensitivity. In the next data release, we will target fainter, and perhaps more distant, H II regions, which may fill in this region of the ℓ-v diagram.

6.1. Survey Completeness

Following the strategy of Anderson et al. (2011), we estimate the completeness of the Bright Catalog to be the point at which the flux density distribution of SHRDS nebulae begins to deviate from a power law. Assuming that the Galactic H II region luminosity function is a power law (e.g., Smith & Kennicutt 1989; McKee & Williams 1997) and that the distribution of nebulae is relatively smooth across the disk, the distribution of H II region flux densities should be a power law as well. In this data release, we only measure peak flux densities. These flux densities will underestimate the total flux densities of resolved sources and, therefore, this analysis is not a representation of the true H II region luminosity function. In the next data release, we will measure the total flux densities of all SHRDS nebulae and reassess the SHRDS completeness limit.

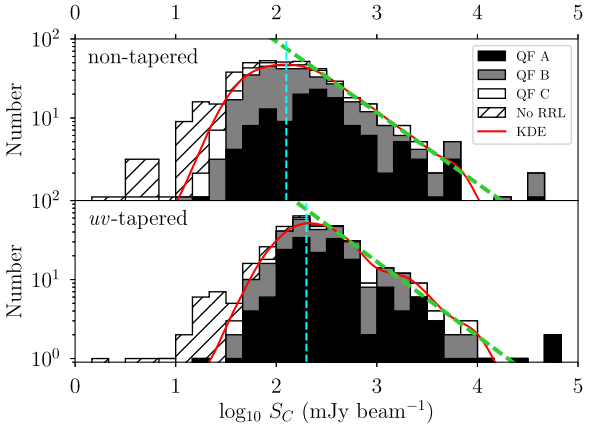

Figure 10. Distribution of peak continuum flux densities for the non-tapered (top) and *uv*-tapered (bottom) SHRDS data. The shaded regions represent the contribution from sources of each continuum QF with a detected RRL (QF A in black, QF B in gray, and QF C in white), and the hatched regions represent the contribution from sources without a detected RRL. The red curves are the Gaussian kernel density estimator (KDE) fits to the distributions, and the green dashed curves are the power laws fit to a subset of the KDEs. The vertical cyan dashed lines represent the estimated continuum completeness limit of the SHRDS: 125 mJy beam^{-1} (non-tapered) and 200 mJy beam^{-1} (tapered) at ∼7 GHz.

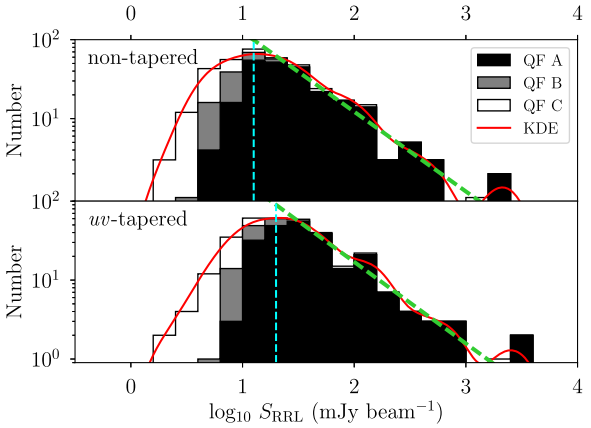

Figure 11. Distribution of $\langle \mathrm{H}n\alpha \rangle$ RRL flux densities (see Figure 10). We estimate the ∼7 GHz RRL completeness to be 12.5 mJy beam^{-1} in the non-tapered data and 20 mJy beam^{-1} in the *uv*-tapered data.

Figure 10 shows the distribution of SHRDS peak continuum flux densities in both the non-tapered and *uv*-tapered data. Both distributions follow a power law at the brighter end. We estimate the completeness of the continuum catalog as the point when these distributions begin to deviate from a power law: ∼125 mJy beam^{-1} in the non-tapered catalog and ∼200 mJy beam^{-1} in the *uv*-tapered catalog. Similar distributions are shown in Figure 11 for the distribution of $\langle \mathrm{H}n\alpha \rangle$ RRL flux densities. The completeness of the RRL catalog as inferred from these distributions is 10 times lower than that of the continuum catalog, as expected for a typical RRL-to-continuum intensity ratio of 0.1 at these frequencies.

Our non-tapered completeness limit (∼125 mJy beam^{-1}) is more than twice our target selection criterion (60 mJy beam^{-1}). This difference is likely due to the uncertainty in extrapolating H II region flux densities from SUMSS 843 MHz to 6 GHz. Figure 12 shows the fractional difference between the measured and predicted peak continuum flux densities for both our non-tapered and *uv*-tapered catalogs. Here, the SHRDS continuum

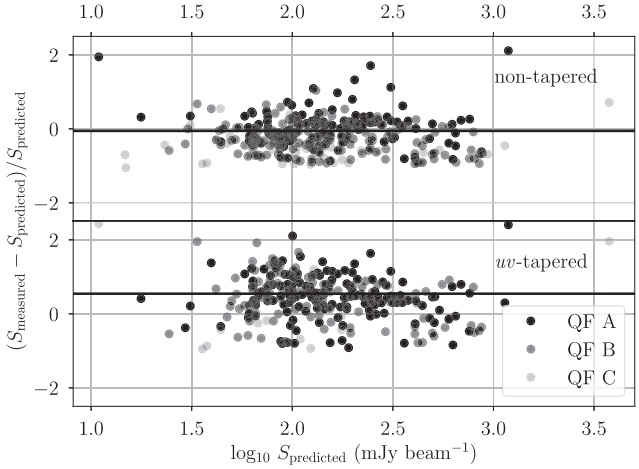

Figure 12. Fractional difference between the measured 6 GHz peak continuum flux densities and the predicted flux densities, as extrapolated from SUMSS. There are 313 non-tapered continuum detections (top) and 278 *uv*-tapered continuum detections (bottom) with SUMSS predicted fluxes in the *WISE* Catalog. Five sources with differences >250% are excluded from each sample for clarity. The SHRDS peak continuum flux densities are extrapolated from their measured frequencies to 6 GHz, assuming a spectral index of $\alpha = -0.1$. The transparency of the points represents the continuum quality factor of the detection: QF A (opaque), QF B (slightly transparent), and QF C (mostly transparent). The horizontal solid lines indicate the mean fractional difference: −6% (non-tapered) and 54% (*uv*-tapered).

fluxes are scaled from their observed frequencies to 6 GHz, assuming a spectral index of $\alpha = -0.1$. The mean difference for the non-tapered data is −6% (overpredicted) and for the *uv*-tapered data is 54% (underpredicted). In both cases, the standard deviation is ∼100%. Anderson et al. (2011) found a similar scatter when extrapolating from ∼1.4 to 10 GHz. This suggests that many H II regions are optically thick at and below 1.4 GHz.

7. Summary and Future Work

The SHRDS has already nearly doubled the number of known Galactic H II regions in the longitude range $259° < \ell < 344°$. In this first data release, the Bright Catalog, we report the detection of 256 new nebulae. We observe 282 fields and find continuum emission toward H II regions or H II region candidates in 275 (97.5%) and RRL emission in 258 (91.5%) of them. We estimate that the SHRDS Bright Catalog is complete for all H II regions with 7 GHz peak continuum flux densities brighter than 125 mJy beam^{-1} in the surveyed zone.

We detect RRL emission from 76 previously known H II regions and find that the SHRDS RRL properties are similar to previous measurements. The mean LSR velocity difference between our measurements and those in the *WISE* Catalog is 1.1 km s^{-1} with a standard deviation of 3.2 km s^{-1}. This scatter is likely due to the velocity resolution of the SHRDS and previous observations. The mean FWHM line width difference is 3% with a standard deviation of 30%. All previous H II region surveys used single-dish telescopes, thus the scatter in FWHM line width differences is likely to be a consequence of the different spatial scales probed by the ATCA.

The distribution of SHRDS line widths is nearly identical to that of all previously known H II regions in the *WISE* Catalog. The physical conditions, such as internal turbulence, of SHRDS H II regions are thus similar to those of the Galactic population of H II regions as a whole.

In this data release, we provide only the positions, continuum flux densities, and stacked $\langle \mathrm{H}n\alpha \rangle$ RRL properties for our sample of bright H II regions. Much more insight will be gained by looking at the intermediate data products, such as the continuum spectral energy distributions, RRL spectral energy distributions, RRL-to-continuum intensity ratio distributions, etc. The next SHRDS data release will add ∼200 more H II regions to the SHRDS catalog, bringing the total number of newly discovered nebulae to ∼500. We will also publish the intermediate data products that will allow for a more detailed analysis of individual H II regions.

A complete catalog of Galactic H II regions in the third and fourth Galactic quadrants will drastically improve our understanding of Galactic high-mass star formation, spiral structure, and metallicity structure. With H I emission/absorption observations toward these newly discovered H II regions, we will resolve the kinematic distance ambiguity of a subset of our sample and create the most complete face-on map of Galactic H II regions to date.

T.V.W. is supported by the NSF through the Grote Reber Fellowship Program administered by Associated Universities, Inc./National Radio Astronomy Observatory, the D.N. Batten Foundation Fellowship from the Jefferson Scholars Foundation, the Mars Foundation Fellowship from the Achievement Rewards for College Scientists Foundation, and the Virginia Space Grant Consortium. L.D.A. is supported in part by NSF grant AST-1516021. T.M.B. is supported in part by NSF grant AST-1714688. J.R.D. is the recipient of an Australian Research Council (ARC) DECRA Fellowship (project number DE170101086). J.S. is supported by the NRAO National Astronomy Consortium (NAC).

The Green Bank Observatory and National Radio Astronomy Observatory are facilities of the National Science Foundation operated under cooperative agreement by Associated Universities, Inc.

The Australia Telescope Compact Array is part of the Australia Telescope National Facility, which is funded by the Australian Government for operation as a National Facility managed by CSIRO.

We thank the anonymous referee for their valuable comments and suggestions, which improved the quality of this paper.

Facility: ATCA.

Software: Astropy (Astropy Collaboration et al. 2013), CASA (McMullin et al. 2007), Matplotlib (Hunter 2007), NumPy & SciPy (van der Walt et al. 2011), Python (https://www.python.org/), WISP (Wenger 2018a).

Appendix A
WISP: A General Radio Interferometry Data Reduction Package

Here, we introduce the data reduction and analysis tools developed for the SHRDS: WISP (Wenger 2018a). WISP is a collection of *Python* code implemented through the CASA package (McMullin et al. 2007). Its generic and modular framework is designed to handle any continuum or spectral line radio interferometry data. We are motivated to create our own data reduction pipeline for three reasons: (1) the large quantity of data in the SHRDS, (2) missing functionality in CASA, and (3) the lack of automatically generated quality diagnostics in existing pipelines.

Our primary motivation for WISP is the overwhelmingly large quantity of data produced in the SHRDS. The calibration process for a single ∼8 hr observing session of the SHRDS, for example, takes ∼16 hr of raw computing time on a reasonably powerful machine, not including the downtime between individual calibration tasks, while inspecting the data, etc. Including this overhead, the entire calibration process for a single observing session can take a week if done interactively. This is impractical considering the hundreds of hours of data accumulated by the SHRDS. With WISP, all of the calibration steps are automated so that there is no downtime between the completion of one task and the start of the next. The total time it takes to calibrate a single observing session using WISP is reduced to only ∼24 hr, including the manual data inspection.

The imaging process is equally as time consuming if done interactively. To *CLEAN* a single spectral line window data cube for a single field can take ∼15 minutes. Given the ∼300 fields and ∼20 spectral line windows, the total computation time required to generate all of the images for the SHRDS Bright Catalog is nearly two months. Interactive cleaning (i.e., determining *CLEAN* masks by hand) would add substantially to the imaging time, so WISP uses automatic *CLEAN* mask generation and other tricks to automate the entire imaging process.

The SHRDS Bright Catalog data grows from about 10 terabytes in its raw form to nearly 50 terabytes after each field and spectral window are imaged ("data reduction" should really be called "data expansion" when discussing radio interferometry). All of the images and data cubes generated for a single source total about 150 gigabytes. WISP (via CASA) generates several intermediate images and data cubes for each field and spectral window, most of which are not needed for the final data analysis. By converting the required images and cubes to Flexible Image Transport System (FITS) files and by deleting all CASA-generated images and cubes, we reduce the disk space for a single source to about 30 gigabytes.

Our second motivation for WISP is a lack of some required functionality in CASA. For example, CASA cannot interpolate through missing or flagged data. The ATCA correlator, CABB, has several known bad channels ("birdies"). If these channels are flagged throughout all of the data, CASA fails to account correctly for the missing data when regridding the velocity axis of our spectral line windows. This failure produces large, periodic ripples in the spectra. WISP has the functionality to interpolate seamlessly through any known bad channels by directly editing the visibility data. Without missing data, the velocity axis regridding works correctly.

Finally, existing pipelines (at least those that existed when the SHRDS began) lack the ability to generate calibration automatically and imaging diagnostics to assess the quality of the data reduction process. For example, after the calibration process, we wish to inspect the derived calibration solutions and the calibrated visibilities. In CASA, this requires the user to run a task, wait (sometimes several minutes) for the plot(s) to be generated, inspect the plots, then repeat for the next calibration solution or visibility set. In total, this can take several hours depending on the number of calibrator sources and calibration solutions to inspect. WISP automatically generates all of the necessary calibration solution and visibility plots and compiles them into a single document. We can then quickly scroll through the plots and identify any issues.

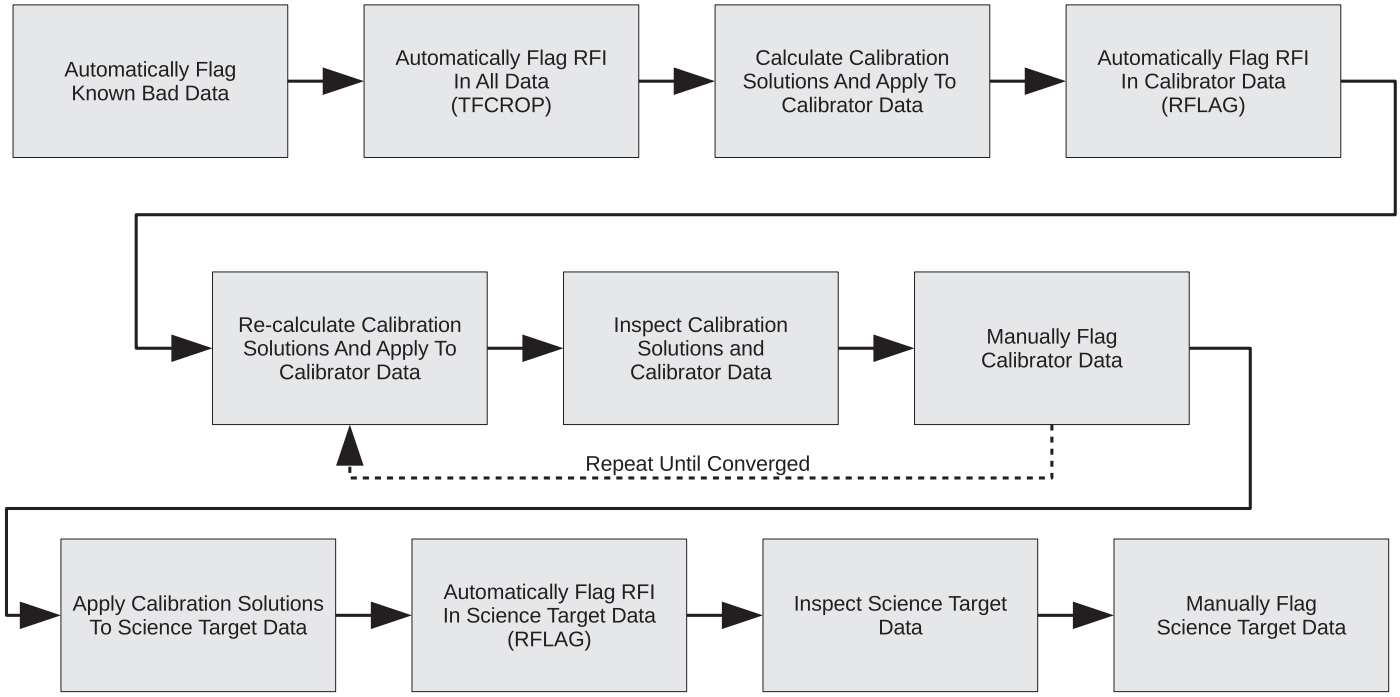

Figure 13. Steps performed by the WISP calibration pipeline.

Below we describe, in detail, the specific calibration and imaging steps performed by WISP.

A.1. Calibration

The calibration pipeline in WISP handles all of the necessary calibration steps: (1) flags bad data, (2) computes calibration solutions, and (3) applies calibration solutions. Using a combination of automated flagging and manual flagging, this pipeline is extremely time-efficient. A summary of the calibration process is shown in Figure 13.

The raw data are contaminated by several sources of bad data, including bad channels in the correlator ("birdies"), shadowed antennas, the beginning and end of scans when the antennas are not on source, and RFI. The pipeline begins by flagging the known sources of bad data: birdies, shadowed antennas, and off-source antennas. We then use the automatic flagging algorithm *TFCROP*, as implemented in CASA, to catch any RFI. This task is the recommended auto-flagging task to use on uncalibrated data by detecting outliers in the time-frequency domain. Our tests show that *TFCROP* is excellent at finding $\sim$95% of bright, short-duration, limited-frequency RFI but often misses complex RFI, which can completely compromise the data quality of a spectral line window.

The data are now pruned of obvious RFI, but some low-level RFI may still remain. Using the calibrator data, we compute preliminary calibration solutions for the absolute flux, bandpass, delays, and complex gains. We apply these calibration solutions to the calibrators, thereby removing any instrumental effects from the data. These calibrated data should be well-behaved, and thus, it is easier to identify any RFI or otherwise bad data. Using the CASA algorithm *RFLAG*, we again automatically flag the calibrator data to identify any remaining bad data. This algorithm differs from *TFCROP* in that it requires the data to be calibrated. It then computes statistics on small chunks of the data and flags data using a threshold determined by these statistics. The *RFLAG* algorithm successfully flags most of the RFI missed by *TFCROP*, but it often misses other bad data, such as misbehaving antennas or RFI compromising an entire spectral line window. This algorithm will also flag the peak of our spectral lines if the spectral line is very bright ($\gtrsim$500 mJy beam^{-1}). In these cases, we must manually unflag the spectral lines.

At this stage, we have run the data through two independent automatic flagging algorithms. We recompute and reapply the calibration solutions. We then generate diagnostic plots to inspect the quality of the calibrator data and calibration solutions. These diagnostic plots are slices of the data in many dimensions: for example, complex amplitude as a function of complex phase, real amplitude as a function of time, and complex phase as a function of frequency. If we notice any heretofore unidentified bad data, we manually flag it, recalculate and reapply the calibration solutions, regenerate the diagnostic plots, and reinspect them. We iterate this process until the calibrator data are free of any bad data.

After accurate calibration solutions are established, the science target data can be calibrated. Using the final calibration solutions, we calibrate the absolute flux, bandpass, delay, and complex gain of the science target data using the secondary calibrator located closest to the science target on the sky. We then run the *RFLAG* algorithm on the science target data to identify any RFI. Finally, we generate diagnostic plots for the science target data and manually flag any remaining bad data.

The final data products generated by the WISP calibration pipeline are: (1) fully calibrated visibilities, (2) a flag table identifying all of the flagged data, (3) the final calibration solution tables, (4) the final diagnostic plots, and (5) a copy of the fully calibrated visibilities for each individual field. We use WISP to calibrate each observing session of the SHRDS. If a given field is observed in multiple sessions, we combine all of the data for that field before imaging.

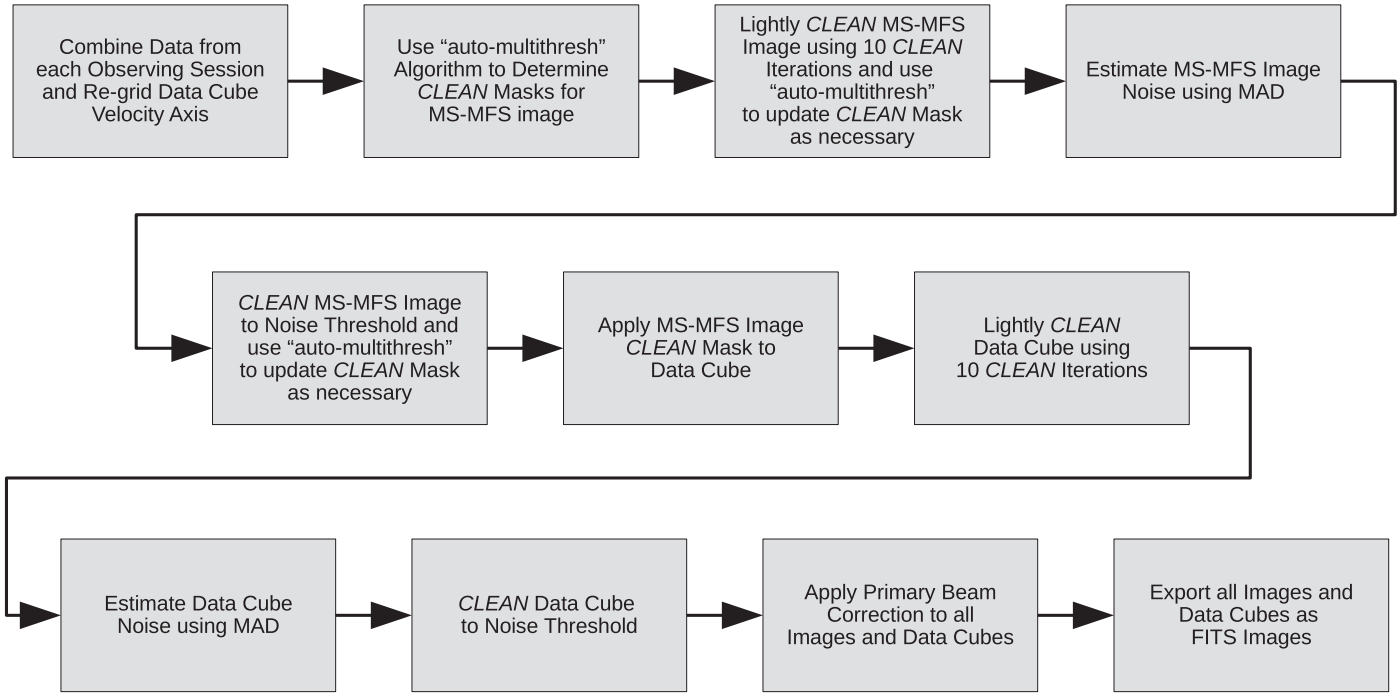

Figure 14. Steps performed by the WISP imaging pipeline for a single spectral line window.

A.2. Imaging

The imaging pipeline in WISP automatically creates several images for each of our fields. This automation is necessary due to the large amount of computing time required to image and to *CLEAN* each field. The *CLEAN* and other imaging parameters are initially set by the user and then applied to every image. All of the imaging and *CLEAN*ing is performed using the CASA task *TCLEAN*. We generate the following images for each field: (1) an MS-MFS image produced by combining the two 2 GHz continuum windows, (2) an MS-MFS image of each 2 GHz bandwidth continuum window, (3) MS-MFS images of each 64 MHz bandwidth spectral line window, and (4) multiscale data cubes of each spectral line window. Figure 14 summarizes the imaging process for a single spectral line window.

We use the newly implemented "auto-multithresh" algorithm to determine *CLEAN* masks automatically in our images (A. Kepley et al. 2019, in preparation). This algorithm applies user-defined thresholds to determine the locations of "real" emission around which to place a *CLEAN* mask. It first masks any emission brighter than a given threshold above the brightest sidelobe in the image, based on the *TCLEAN*-generated dirty beam image. After several iterations of *CLEAN* , the dirty beam sidelobes are suppressed and the algorithm begins masking any emission brighter than a given threshold above the estimated noise in the *TCLEAN*-generated residual image. The sidelobe masking threshold is very sensitive to the *uv*-coverage of the data; images with very complete *uv*-coverage, either because of large bandwidths or more hour angle coverage, have dirty beams with lower sidelobes, whereas images with poor *uv*-coverage may have sidelobes comparable in gain to the synthesized beam. Therefore, we use a separate set of thresholds for the large-bandwidth continuum windows and the small-bandwidth spectral line windows.

The "auto-multithresh" algorithm is time consuming when applied to each channel of a data cube independently. We reduce the *CLEAN* computation time by applying the "auto-multithresh" *CLEAN* mask from the MS-MFS image of a given spectral window to all of the channels in the data cube for that spectral window. This is possible because the morphology of our target H II regions and H II region candidates should not change from channel to channel; the free–free continuum and RRL emission originate in the same volume of gas.

Each image and data cube is "lightly *CLEAN* ed" by running only 10 iterations of *CLEAN* . From these data we estimate the image noise and *CLEAN* stopping criterion (i.e., *CLEAN* threshold). We compute the median absolute deviation (MAD) of the *TCLEAN*-generated residual image to estimate the *CLEAN* threshold. The MAD is a robust estimator of the noise of a data set even in the presence of outliers. For Gaussian noise, MAD is related to the root-mean-square, rms, by rms $\simeq$ 1.4826 MAD. We use this rms as the stopping criterion for *CLEAN* : when the maximum absolute value of the residual image within the *CLEAN* mask is below this value, we stop *CLEAN*. This entire process usually takes fewer than 50 iterations of *CLEAN* for the MS-MFS images and 200 iterations for the spectral data cubes.

In order to average together each spectral window into a final $\langle \mathrm{H}n\alpha \rangle$ spectrum, we must regrid the spectral windows to a common velocity frame. Using the CASA task *CVEL2*, we linearly interpolate each spectral line window to the kinematic local standard of rest (LSRK) reference frame in 321 velocity channels with a 2.5 km s^{-1} width starting at -400 km s^{-1}. This gives us velocity coverage from $V_{\mathrm{LSR}} = -400$ km s^{-1} to $+400$ km s^{-1}, sufficient to detect all Galactic H II regions.

Finally, each image and data cube is primary beam corrected. We divide each image and cube by the *TCLEAN*-generated primary beam image. For our full 4 GHz bandwidth continuum images, we use the CASA task *WIDEBANDPBCOR* which considers the varying primary beam over a large fractional bandwidth (4–10 GHz in our case). For all other images, we

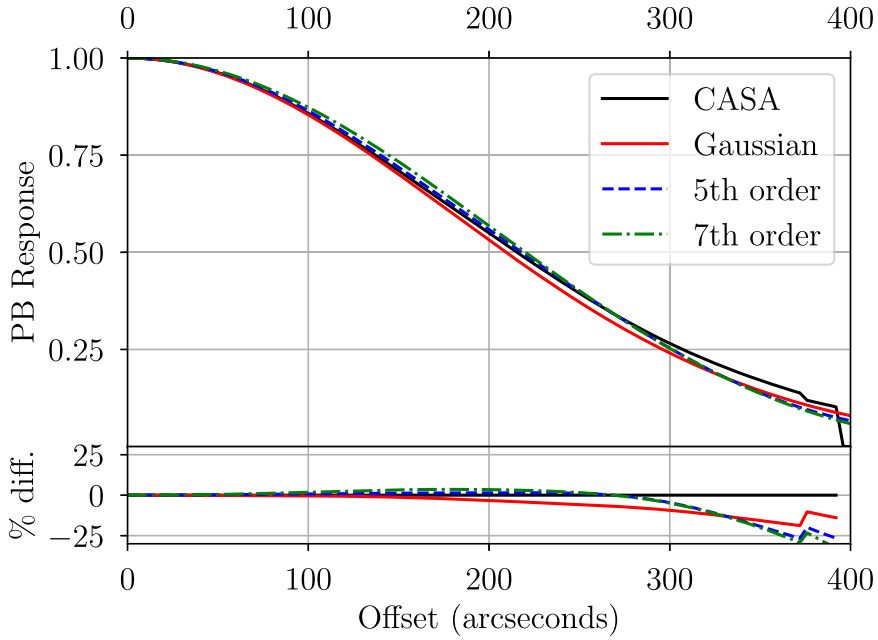

Figure 15. The primary beam response generated by *TCLEAN* (black solid line) and three empirical models by Wieringa & Kesteven (1992): a Gaussian (red solid line), a 5th order polynomial (blue dashed line), and a 7th order polynomial (green dashed–dotted line). The bottom panel shows the percent difference between the three Wieringa & Kesteven (1992) models and the *TCLEAN*-generated profile.

use *IMPBCOR* which applies the primary beam correction using the primary beam of the center frequency. Figure 15 shows the *TCLEAN*-generated primary beam profile for a 4 GHz bandwidth MS-MFS image. We also show the Gaussian, 5th order polynomial, and 7th order polynomial empirical primary beam models from Wieringa & Kesteven (1992). The CASA primary beam deviates significantly ($\gtrsim$10%) from these models beyond $\sim$300 arcsec from the primary beam center. Thus the continuum and RRL intensities of sources at the edges of an observed field are inaccurate.

The final data products generated by the WISP imaging pipeline for each field are: (1) an MS-MFS image of the combined 4 GHz bandwidth continuum windows, (2) an MS-MFS image of each 2 GHz bandwidth continuum window, (3) MS-MFS images of each 64 MHz bandwidth spectral line window, and (4) multiscale data cubes of each spectral line window. These images are saved both as CASA and FITS images. All subsequent analyses are performed using the FITS images, so the CASA images are deleted.

Appendix B
Multiple Detections

A *WISE* Catalog source may appear in multiple fields. The data with the highest quality factor and/or the largest S/N is included in the main catalogs (Tables 4–7). Here we give the radio continuum and $\langle$H$n\alpha\rangle$ RRL properties for these "multiple detections" as measured in each independent field. Most of these sources are located near the edge of the field, so the continuum and RRL intensities may be inaccurate (see Appendix A). The data in the main catalogs, not the multiple detections catalogs, should be used for all subsequent analyses. In the next data release, we will combine the data from each field to improve our sensitivity and to measure the continuum and RRL properties of these sources more accurately.

The continuum properties of the multiple detections are listed in Table 8 (non-tapered) and Table 9 (*uv*-tapered). For each source, we list the *WISE* Catalog name; the position of the peak radio continuum emission; the fields containing the source; the epoch; the synthesized beam area in the continuum image; the separation between the observed continuum peak position and infrared position, $\Delta\theta$; the MFS-synthesized frequency of the continuum image, ν_C; the peak continuum flux density, S_C; the rms noise, rms$_C$; and a QF. These tables contain one row for each field in which the source is found.

The $\langle$H$n\alpha\rangle$ RRL properties of the multiple detections are listed in Table 10 (non-tapered) and Table 11 (*uv*-tapered). For each source, we give the *WISE* Catalog name; the field; the epoch; the weighted-average frequency of the $\langle$H$n\alpha\rangle$ RRL, ν_L; the Gaussian fits to the peak intensity, S_L; the LSR velocity, $V_{\rm LSR}$, and the FWHM line width, ΔV; the rms spectral noise in the line-free region of the spectrum, rms$_L$; the S/N; and a QF. These tables also contain one row for each field in which the source is found.

Table 8
Non-tapered Image Continuum Properties of Multiple Detections

Target	R.A. J2000 (hh:mm:ss)	Decl. J2000 (dd:mm:ss)	Field	Epoch[a]	Beam Area (arcsec^2)	$\Delta\theta$[b] (arcsec)	ν_C (MHz)	S_C (mJy beam^{-1})	rms$_C$ (mJy beam^{-1})	QF
G289.944−00.889	11:01:11.1	−60:56:48.0	shrds191	2015	2502	10.2	7023	123.68	1.47	A
G289.944−00.889	11:01:09.7	−60:56:40.8	g290.012-00.867	2014	5394	16.4	6050	135.43	7.10	C
G290.012−00.867	11:01:59.2	−60:56:48.8	g290.012-00.867	2014	5394	106.4	6050	200.17	3.66	B
G290.012−00.867	11:01:45.4	−60:57:25.8	g290.012-00.867	2014*	⋯	0.8	⋯	⋯	⋯	⋯
G290.323−02.984	10:56:33.0	−63:00:43.9	g290.323-02.984	2014	5453	26.8	6050	28.85	0.34	A
G290.323−02.984	10:56:36.4	−63:00:35.0	g290.323-02.984	2014*	⋯	2.9	⋯	⋯	⋯	⋯
G290.385−01.042	11:03:59.6	−61:16:04.4	g290.385-01.042	2014	5384	2.0	6050	23.30	0.87	A
G290.385−01.042	11:03:59.4	−61:16:06.7	g290.385-01.042	2014*	⋯	0.6	⋯	⋯	⋯	⋯

Notes.
[a] Rows with epochs with an asterisk (*) are copied directly from Brown et al. (2017). They did not give the continuum fluxes for their detections.
[b] The separation between the *WISE* Catalog infrared position and the position of the SHRDS continuum peak.

(This table is available in its entirety in machine-readable form.)

Table 9
uv-tapered Image Continuum Properties of Multiple Detections

Target	R.A. J2000 (hh:mm:ss)	Decl. J2000 (dd:mm:ss)	Field	Epoch[a]	Beam Area (arcsec^2)	$\Delta\theta$[b] (arcsec)	ν_C (MHz)	S_C (mJy beam^{-1})	rms$_C$ (mJy beam^{-1})	QF
G289.944−00.889	11:01:11.1	−60:56:48.0	shrds191	2015	9232	10.1	7023	145.89	3.69	A
G289.944−00.889	11:01:09.7	−60:56:44.3	g290.012-00.867	2014	7104	13.1	6050	131.86	10.48	B
G290.012−00.867	11:01:59.1	−60:56:49.2	g290.012-00.867	2014	7104	105.8	6050	196.21	5.43	B
G290.012−00.867	11:01:45.4	−60:57:25.8	g290.012-00.867	2014*	⋯	0.8	⋯	⋯	⋯	⋯
G290.323−02.984	10:56:33.0	−63:00:44.2	g290.323-02.984	2014	7202	27.2	6050	29.11	0.46	A
G290.323−02.984	10:56:36.4	−63:00:35.0	g290.323-02.984	2014*	⋯	2.9	⋯	⋯	⋯	⋯
G290.385−01.042	11:03:59.5	−61:16:04.9	g290.385-01.042	2014	7084	1.4	6050	24.97	1.35	A
G290.385−01.042	11:03:59.4	−61:16:06.7	g290.385-01.042	2014*	⋯	0.6	⋯	⋯	⋯	⋯

Notes.
[a] Rows with epochs with an asterisk (*) are copied directly from Brown et al. (2017). They did not give the continuum fluxes for their detections.
[b] The separation between the *WISE* Catalog infrared position and the position of the SHRDS continuum peak.

(This table is available in its entirety in machine-readable form.)

Table 10
Non-tapered Image RRL Properties of Multiple Detections

Target	Field	Epoch[a]	ν_L[b] (MHz)	S_L (mJy beam^{-1})	$V_{\rm LSR}$ (km s^{-1})	ΔV (km s^{-1})	rms$_L$ (mJy beam^{-1})	S/N	QF
G289.944−00.889	shrds191	2015	6800	8.60 ± 0.50	31.50 ± 0.70	23.60 ± 1.70	1.40	13.6	B
G289.944−00.889	g290.012-00.867	2014	5193	11.70 ± 3.10	31.80 ± 1.70	13.10 ± 4.20	5.10	3.7	C
G290.012−00.867	g290.012-00.867	2014	6134	⋯	⋯	⋯	3.00	⋯	D
G290.012−00.867	g290.012-00.867	2014*	⋯	3.60 ± 2.50	14.70 ± 8.30	24.90 ± 8.60	1.80	4.5	C
G290.323−02.984	g290.323-02.984	2014	5874	⋯	⋯	⋯	2.50	⋯	D
G290.323−02.984	g290.323-02.984	2014*	⋯	3.50 ± 2.10	−17.70 ± 8.00	28.30 ± 8.30	1.50	5.6	C
G290.385−01.042	g290.385-01.042	2014	5911	⋯	⋯	⋯	2.30	⋯	D
G290.385−01.042	g290.385-01.042	2014*	⋯	4.00 ± 2.90	9.91 ± 4.60	13.20 ± 4.70	1.90	3.4	C

Notes.
[a] Rows with epochs with an asterisk (*) are copied directly from Brown et al. (2017). They did not give the weighted-average frequency of their H$n\alpha$ RRL spectra.
[b] This is the weighted-average frequency of the $\langle$H$n\alpha\rangle$ stacked spectrum.

(This table is available in its entirety in machine-readable form.)

Table 11
uv-tapered Image RRL Properties of Multiple Detections

Target	Field	Epoch[a]	ν_L[b] (MHz)	S_L (mJy beam^{-1})	$V_{\rm LSR}$ (km s^{-1})	ΔV (km s^{-1})	rms$_L$ (mJy beam^{-1})	S/N	QF
G289.944−00.889	shrds191	2015	6429	8.90 ± 0.80	32.30 ± 0.90	21.40 ± 2.10	1.70	11.0	B
G289.944−00.889	g290.012-00.867	2014	5276	⋯	⋯	⋯	4.40	⋯	D
G290.012−00.867	g290.012-00.867	2014	6035	⋯	⋯	⋯	3.00	⋯	D
G290.012−00.867	g290.012-00.867	2014*	⋯	3.60 ± 2.50	14.70 ± 8.30	24.90 ± 8.60	1.80	4.5	C
G290.323−02.984	g290.323-02.984	2014	5819	⋯	⋯	⋯	2.50	⋯	D
G290.323−02.984	g290.323-02.984	2014*	⋯	3.50 ± 2.10	−17.70 ± 8.00	28.30 ± 8.30	1.50	5.6	C
G290.385−01.042	g290.385-01.042	2014	5921	⋯	⋯	⋯	2.40	⋯	D
G290.385−01.042	g290.385-01.042	2014*	⋯	4.00 ± 2.90	9.91 ± 4.60	13.20 ± 4.70	1.90	3.4	C

Notes.
[a] Rows with epochs with an asterisk (*) are copied directly from Brown et al. (2017). They did not give the weighted-average frequency of their Hnα RRL spectra.
[b] This is the weighted-average frequency of the $\langle$H$n\alpha\rangle$ stacked spectrum.

(This table is available in its entirety in machine-readable form.)

ORCID iDs

Trey V. Wenger https://orcid.org/0000-0003-0640-7787
John. M. Dickey https://orcid.org/0000-0002-6300-7459
C. H. Jordan https://orcid.org/0000-0002-1220-2940
Dana S. Balser https://orcid.org/0000-0002-2465-7803
W. P. Armentrout https://orcid.org/0000-0002-7045-9277
L. D. Anderson https://orcid.org/0000-0001-8800-1793
T. M. Bania https://orcid.org/0000-0003-4866-460X
J. R. Dawson https://orcid.org/0000-0003-0235-3347
N. M. McClure-Griffiths https://orcid.org/0000-0003-2730-957X

References

Altenhoff, W. J., Downes, D., Pauls, T., & Schraml, J. 1979, A&AS, 35, 23
Anderson, L. D., Armentrout, W. P., Johnstone, B. M., et al. 2015, ApJS, 221, 26
Anderson, L. D., Armentrout, W. P., Luisi, M., et al. 2018, ApJS, 234, 33
Anderson, L. D., Bania, T. M., Balser, D. S., et al. 2014, ApJS, 212, 1
Anderson, L. D., Bania, T. M., Balser, D. S., & Rood, R. T. 2011, ApJS, 194, 32
Astropy Collaboration, Robitaille, T. P., Tollerud, E. J., et al. 2013, A&A, 558, A33
Bania, T. M., Anderson, L. D., & Balser, D. S. 2012, ApJ, 759, 96
Bania, T. M., Anderson, L. D., Balser, D. S., & Rood, R. T. 2010, ApJL, 718, L106
Becker, R. H., White, R. L., Helfand, D. J., & Zoonematkermani, S. 1994, ApJS, 91, 347
Bihr, S., Johnston, K. G., Beuther, H., et al. 2016, A&A, 588, A97
Bock, D. C.-J., Large, M. I., & Sadler, E. M. 1999, AJ, 117, 1578
Brown, C., Jordan, C., Dickey, J. M., et al. 2017, AJ, 154, 23
Caswell, J. L., & Haynes, R. F. 1987, A&A, 171, 261
Condon, J. J., Cotton, W. D., Greisen, E. W., et al. 1998, AJ, 115, 1693
Downes, D., Wilson, T. L., Bieging, J., & Wink, J. 1980, A&AS, 40, 379
Gum, C. S. 1955, MmRAS, 67, 155
Helfand, D. J., Becker, R. H., White, R. L., Fallon, A., & Tuttle, S. 2006, AJ, 131, 2525
Hoglund, B., & Mezger, P. G. 1965a, Sci, 150, 339
Hoglund, B., & Mezger, P. G. 1965b, AJ, 70, 678
Hunter, J. D. 2007, CSE, 9, 90
Kardashev, N. S. 1959, SvA, 3, 813
Lenz, D. D., & Ayres, T. R. 1992, PASP, 104, 1104
Lockman, F. J. 1989, ApJS, 71, 469
Lockman, F. J., & Brown, R. L. 1975, ApJ, 201, 134
Lockman, F. J., Pisano, D. J., & Howard, G. J. 1996, ApJ, 472, 173
Mauch, T., Murphy, T., Buttery, H. J., et al. 2003, MNRAS, 342, 1117
McClure-Griffiths, N. M., Dickey, J. M., Gaensler, B. M., et al. 2005, ApJS, 158, 178
McKee, C. F., & Williams, J. P. 1997, ApJ, 476, 144
McMullin, J. P., Waters, B., Schiebel, D., Young, W., & Golap, K. 2007, in ASP Conf. Ser. 376, Astronomical Data Analysis Software and Systems XVI, ed. R. A. Shaw, F. Hill, & D. J. Bell (San Francisco, CA: ASP), 127
Reifenstein, E. C., Wilson, T. L., Burke, B. F., Mezger, P. G., & Altenhoff, W. J. 1970, A&A, 4, 357
Rodgers, A. W., Campbell, C. T., & Whiteoak, J. B. 1960, MNRAS, 121, 103
Sharpless, S. 1953, ApJ, 118, 362
Sharpless, S. 1959, ApJS, 4, 257
Smith, T. R., & Kennicutt, R. C., Jr. 1989, PASP, 101, 649
Stil, J. M., Taylor, A. R., Dickey, J. M., et al. 2006, AJ, 132, 1158
Strömgren, B. 1948, ApJ, 108, 242
Taylor, A. R., Gibson, S. J., Peracaula, M., et al. 2003, AJ, 125, 3145
van der Walt, S., Colbert, S. C., & Varoquaux, G. 2011, CSE, 13, 22
Wenger, T. V. 2018a, WISP: Wenger Interferometry Software Package, Astrophysics Source Code Library, ascl:1812.001
Wenger, T. V. 2018b, WISP: Wenger Interferometry Software Package, Zenodo, doi:10.5281/zenodo.2225273
Wieringa, M. H., & Kesteven, M. J. 1992, Measurements of the ATCA Primary Beam TNF Tech. Memo 39.2/010, (Marsfield: Australia Telescope National Facility)
Wilson, T. L., Mezger, P. G., Gardner, F. F., & Milne, D. K. 1970, A&A, 6, 364
Wright, E. L., Eisenhardt, P. R. M., Mainzer, A. K., et al. 2010, AJ, 140, 1868